Supplement of "Contrasting land carbon uptake responses to El Niño–Southern Oscillation across North America"

Wu Sun[1,✉], Kelsey T. Foster[1,2], Yoichi P. Shiga[3], Julian Merder[1], Nina A. Randazzo[4,5], and Anna M. Michalak[1,2]

[1]Department of Global Ecology, Carnegie Institution for Science, Stanford, California, USA

[2]Department of Earth System Science, Doerr School of Sustainability, Stanford University, Stanford, California, USA

[3]Independent Researcher, San Francisco, California, USA

[4]Global Modeling and Assimilation Office, NASA Goddard Space Flight Center, Greenbelt, Maryland, USA

[5]Earth System Science Interdisciplinary Center, University of Maryland, College Park, Maryland, USA

✉Email: wsun@carnegiescience.edu

List of Supplementary Tables

List of Supplementary Figures

Table S1. List of sites that provide atmospheric CO_2 concentration measurements during 2007–2015, compiled from the ObsPack GLOBALVIEWplus CO_2 v3.2 data set. See also Fig. S1 for locations of these monitoring stations.

Code	Name	Latitude	Longitude	Start	End	Height (m)	Principal Investigators
AAC	Austin Cary Memorial Forest, Gainesville, FL, USA	29.7381	−82.2188	2010	2012	32	
ACR	Chestnut Ridge, TX, USA	35.9311	−84.3324	2007	2011	61	
ACV	Canaan Valley, WV, USA	39.1190	−79.4523	2007	2011	7	Natasha Miles, Scott Richardson, & Ken Davis (PSU)
AME	Mead, NE, USA	41.1649	−96.4701	2007	2011	5	
AOZ	Ozark, MO, USA	38.7441	−92.2000	2007	2011	30	
FPK	Fort Peck, MT, USA	48.3079	−105.1017	2007	2008	3	
GCI02	Grenada, MS, USA	33.7525	−89.8539	2015	2015	100	
GCI03	Magee, MS, USA	31.8869	−89.7276	2015	2015	100	
GCI04	Millerville, AL, USA	33.1759	−85.8911	2015	2015	100	
INX01	INFLUX Tower 1, Mooresville, IN, USA	39.5805	−86.4207	2011	2012	121	
INX09	INFLUX Tower 9, Greenfield, IN, USA	39.8627	−85.7448	2012	2012	130	
RCE	Centerville, IA, USA	40.7919	−92.8775	2007	2009	110	
RGV	Galesville, WI, USA	44.0910	−91.3382	2007	2009	140	
RKW	Kewanee, IL, USA	41.2762	−89.9724	2007	2009	140	

continued on the next page

Code	Name	Latitude	Longitude	Start	End	Height (m)	Principal Investigators
continued from the previous page							
RMM	Mead, NE, USA	41.1386	−96.4559	2007	2009	120	
RRL	Round Lake, MN, USA	43.5263	−95.4137	2007	2009	110	
AMT	Argyle, ME, USA	45.0346	−68.6821	2007	2015	107	Arlyn Andrews (NOAA/GML)
BAO	Boulder Atmospheric Observatory, CO, USA	40.0500	−105.0040	2007	2015	300	
LEF	Park Falls, WI, USA	45.9453	−90.2744	2007	2015	396	
WBI	West Branch, IA, USA	41.7248	−91.3529	2007	2015	379	
WKT	Moody, TX, USA	31.3149	−97.3269	2007	2015	457	
SNP	Shenandoah National Park, VA, USA	38.6170	−78.3500	2008	2015	17	Arlyn Andrews (NOAA/GML) & Stephan De Wekker (UVA)
SCT	Beech Island, SC, USA	33.4057	−81.8334	2008	2015	305	Arlyn Andrews (NOAA/GML) & Matt Parker (SRNL)
WGC	Walnut Grove, CA, USA	38.2650	−121.4911	2007	2015	483	Arlyn Andrews (NOAA/GML) & Marc Fischer (LBNL)
BRW	Barrow Atmospheric Baseline Observatory, AK, USA	71.3230	−156.6114	2007	2015	17	Kirk Thoning & Pieter Tans (NOAA/GML)
continued on the next page							

Code	Name	Latitude	Longitude	Start	End	Height (m)	Principal Investigators
continued from the previous page							
MVY	Marthas Vineyard, MA, USA	41.3250	−70.5667	2007	2015	10	Colm Sweeney (NOAA/GML)
ABT	Abbotsford, BC, Canada	49.0113	−122.3360	2014	2015	33	
BCK	Behchoko, NT, Canada	62.7979	−115.9180	2010	2015	60	
BRA	Bratt's Lake, SK, Canada	50.2016	−104.7110	2009	2015	35	
CBY	Cambridge Bay, NU, Canada	69.1284	−105.0580	2012	2015	12	
CDL	Candle Lake, SK, Canada	53.9871	−105.1179	2007	2011	30	Doug Worthy (Environment and Climate Change Canada)
CHL	Churchill, MB, Canada	58.7379	−93.8206	2011	2015	60	
CHM	Chibougamau, QC, Canada	49.6925	−74.3423	2007	2010	30	
CPS	Chapais, QC, Canada	49.8223	−74.9753	2011	2015	8–40	
EGB	Egbert, ON, Canada	44.2310	−79.7838	2007	2015	3	
ESP	Estevan Point, BC, Canada	49.3829	−126.5440	2009	2015	40	
EST	Esther, AB, Canada	51.6700	−110.2060	2010	2015	3	
ETL	East Trout Lake, SK, Canada	54.3537	−104.9870	2007	2015	105	
FNE	Fort Nelson, BC, Canada	58.8412	−122.5740	2014	2015	15	
FSD	Fraserdale, ON, Canada	49.8752	−81.5698	2007	2015	40	
continued on the next page							

Code	Name	Latitude	Longitude	Start	End	Height (m)	Principal Investigators
continued from the previous page							
HNP	Hanlan's Point, ON, Canada	43.6121	−79.3862	2014	2015	10	
INU	Inuvik, NT, Canada	68.3178	−133.5340	2012	2015	10	
LLB	Lac La Biche, AB, Canada	54.9538	−112.4670	2007	2015	10	
TPD	Turkey Point, ON, Canada	42.6365	−80.5547	2012	2015	35	
WSA	Sable Island, NS, Canada	43.9323	−60.0126	2007	2015	25	
HFM	Harvard Forest, MA, USA	42.5378	−72.1714	2010	2015	29	Steve Wofsy & Bill Munger (Harvard)
SGP	Southern Great Plains, OK, USA	36.6070	−97.4890	2007	2015	60	Sebastien Biraud & Margaret Torn (LBNL)
HDP	Hidden Peak, UT, USA	40.5600	−111.6500	2007	2015	18	Britton Stephens (NCAR)
NWR	Niwot Ridge, CO, USA	40.0531	−105.5864	2007	2015	5	
RBA	Roof Butte, AZ	36.4614	−109.0956	2007	2014	22	
SPL	Storm Peak Laboratory, CO, USA	40.4500	−106.7300	2007	2015	9	
OFR	Fir, OR, USA	44.6465	−123.5514	2007	2010	38	Beverly Law (Oregon State U)
OMP	Mary's Peak, OR, USA	44.5043	−123.5530	2007	2015	10	
OMT	Meolius, OR, USA	44.4524	−121.5572	2007	2015	33	
ONG	Burns, OR, USA	43.4704	−119.6910	2007	2015	6	
continued on the next page							

Code	Name	Latitude	Longitude	Start	End	Height (m)	Principal Investigators
continued from the previous page							
OSI	Silverton, OR, USA	44.9986	−122.6950	2012	2015	269	
OWA	Walton, OR, USA	44.0664	−123.6290	2012	2015	72	
OYQ	Yaquina Head, OR, USA	44.6750	−124.0670	2007	2011	12	
KCMP	Rosemount Research and Outreach Center, MN, USA	44.6886	−93.0728	2007	2008	200	Tim Griffis (UMN)
CRV	Carbon in Arctic Reservoirs Vulnerability Experiment (CARVE)	64.9863	−147.5980	2011	2015	32	Colm Sweeney, Arlyn Andrews, John B. Miller, & Kathryn McKain (NOAA/GML)
MBO	Mt. Bachelor Observatory, OR, USA	43.9775	−121.6861	2012	2015	11	Dan Jaffe (UW) & Arlyn Andrews (NOAA/GML)

Table S2. Number of atmospheric CO_2 observations assimilated each year.

Year	Number of observations
2007	8851
2008	9923
2009	9956
2010	10,587
2011	10,204
2012	11,451
2013	11,282
2014	11,728
2015	12,381
Total	96,363

Table S3. Drift coefficients of explanatory variables used in geostatistical inverse estimation of carbon fluxes: solar-induced fluorescence (SIF), specific humidity (q), and precipitation. Also shown are standard errors (SE) of estimated drift coefficients. Units of drift coefficients are: $\hat{\beta}_{\text{SIF}}$, $\mu\text{mol}\,\text{s}^{-1}\,\text{mW}^{-1}\,\text{sr}\,\text{nm}$; $\hat{\beta}_q$, $\mu\text{mol}\,\text{m}^{-2}\,\text{s}^{-1}\,\text{kg}^{-1}\,\text{H}_2\text{O}\,\text{kg air}$, $\hat{\beta}_{\text{precip}}$, $\mu\text{mol}\,\text{kg}^{-1}$.

	$\hat{\beta}_{\text{SIF}}$	$\text{SE}(\hat{\beta}_{\text{SIF}})$	$\hat{\beta}_q$	$\text{SE}(\hat{\beta}_q)$	$\hat{\beta}_{\text{precip}}$	$\text{SE}(\hat{\beta}_{\text{precip}})$
2007	−1.329	0.127	109.8	16.5	4037.4	1306.9
2008	−1.339	0.124	164.9	17.0	1658.7	1182.7
2009	−1.876	0.116	177.6	15.5	−339.8	1047.1
2010	−1.185	0.119	97.0	16.3	−2259.7	873.8
2011	−1.385	0.127	134.0	15.9	868.0	934.8
2012	−1.347	0.115	100.5	14.4	589.6	975.7
2013	−1.015	0.110	71.0	13.8	349.2	1014.2
2014	−1.698	0.142	105.4	13.8	−327.2	870.2
2015	−1.219	0.126	98.7	12.4	977.6	823.8

Table S4. Optimized sill variance (σ^2_Q, $[\mu mol\, m^{-2}\, s^{-1}]^2$) for each month. The 2007–2015 mean values for each month are used for inverse estimation of CO_2 fluxes.

	2007	2008	2009	2010	2011	2012	2013	2014	2015	Mean
January	2.1	20.7	2.5	2.2	5.0	4.2	3.2	2.1	1.0	4.8
February	2.7	6.0	1.7	2.0	5.2	1.5	1.2	1.9	2.1	2.7
March	10.7	12.9	6.6	4.1	3.7	2.6	2.3	4.1	2.7	5.5
April	6.2	9.0	6.5	14.8	6.1	3.6	4.7	4.1	3.4	6.5
May	17.7	17.5	18.5	18.0	4.6	2.4	6.0	19.9	11.9	12.9
June	38.8	40.8	40.7	22.4	16.6	23.8	39.0	22.5	38.1	31.4
July	89.3	72.8	93.8	44.0	40.5	27.7	61.4	53.8	58.0	60.1
August	69.2	53.5	70.4	18.5	38.5	15.5	30.8	21.5	42.4	40.0
September	29.8	17.9	26.5	8.6	8.8	8.9	20.5	14.5	13.8	16.6
October	11.8	27.4	8.9	5.3	3.5	5.0	4.0	5.2	7.1	8.7
November	5.4	7.7	6.9	5.9	2.2	3.7	3.3	2.7	5.1	4.8
December	4.1	8.1	2.7	2.8	2.2	1.8	3.1	1.3	1.9	3.1

Table S5. Spatial correlation length (ℓ, km) for each month. The 2007–2015 mean values for each month are used for the inverse estimates of CO_2 fluxes.

	2007	2008	2009	2010	2011	2012	2013	2014	2015	Mean
January	1006	6983	466	775	4217	4012	1024	591	1151	2247
February	9530	1375	507	1498	1622	5993	279	1234	1352	2599
March	941	9988	477	302	1362	1196	831	1770	1318	2021
April	1049	1012	639	2073	842	2393	1303	979	610	1211
May	784	1282	641	2232	1901	746	793	1152	284	1091
June	1162	1378	1308	1627	2648	1797	181	220	470	1199
July	624	1816	2450	781	1480	1880	455	250	151	1099
August	613	673	1135	969	1438	559	891	560	783	847
September	926	1412	1475	2082	992	1454	530	720	655	1138
October	828	3866	542	2465	1119	2198	504	1069	1001	1510
November	1424	799	3561	4386	936	1632	1100	944	1419	1800
December	391	438	401	812	863	1344	439	212	2050	772

Table S6. Temporal correlation length (τ, d) for each month. The 2007–2015 mean values for each month are used for the inverse estimates of CO_2 fluxes.

	2007	2008	2009	2010	2011	2012	2013	2014	2015	Mean
January	10	44	15	31	78	23	51	16	60	37
February	57	28	20	42	24	77	60	60	60	48
March	79	89	10	15	13	21	31	60	49	41
April	73	11	30	70	28	100	28	47	20	45
May	20	46	6	100	17	100	60	60	32	49
June	56	53	30	23	100	100	20	30	43	51
July	23	60	50	18	89	100	12	45	45	49
August	43	48	19	19	97	25	28	25	17	35
September	28	5	6	47	8	19	8	22	11	17
October	14	18	10	61	57	57	4	60	7	32
November	15	18	100	68	96	99	60	33	41	59
December	8	9	3	25	45	33	60	60	60	34

Table S7. List of terrestrial biosphere models from the TRENDY v11 ensemble (Friedlingstein et al., 2022) used in this study.

Model	Full name	References
CABLE-POP	Community Atmosphere–Biosphere Land Exchange model + Populations–Order–Physiology model	Haverd et al. (2018)
CLASSIC	Canadian Land Surface Scheme Including Biogeochemical Cycles	Melton et al. (2020)
CLM5.0	Community Land Model Version 5	Lawrence et al. (2019)
IBIS	Integrated Biosphere Simulator	Yuan et al. (2014)
ISAM	Integrated Science Assessment Model	Meiyappan et al. (2015)
ISBA-CTRIP	Interaction Soil-Biosphere-Atmosphere (ISBA) & Centre National de Recherches Météorologiques Total Runoff Integrating Pathways (CTRIP)	Delire et al. (2020)
JSBACH	Jena Scheme for Biosphere-Atmosphere Coupling in Hamburg	Reick et al. (2021)
JULES	Joint UK Land Environment Simulator	Wiltshire et al. (2021)
LPJ	Lund–Potsdam–Jena Model	Poulter et al. (2011)
LPX-Bern	Land Surface Processes and Exchanges Model	Lienert and Joos (2018)
OCN	Organising Carbon and Hydrology in Dynamic Ecosystems (with Carbon–Nitrogen Coupling)	Zaehle and Friend (2010)
ORCHIDEEv3	Organising Carbon and Hydrology in Dynamic Ecosystems (Version 3; Revision 7267)	Vuichard et al. (2019)
SDGVM	Sheffield Dynamic Global Vegetation Model	Walker et al. (2017)
VISIT	Vegetation Integrative Simulator for Trace Gases	Kato et al. (2013)
VISIT-NIES	Vegetation Integrative Simulator for Trace Gases (National Institute for Environmental Studies, Japan)	Ito (2019)
YIBs	The Yale Interactive terrestrial Biosphere model	Yue and Unger (2015)

Table S8. Attribution of carbon uptake anomalies to concurrent or lag-1 climate anomalies in ENSO-sensitive regions. We use the Schwarz Bayesian information criterion (SBC) to select climate anomalies that best explain carbon uptake anomalies among anomalies in temperature (ΔT), solar radiation (ΔR_{sw}), precipitation (ΔP), soil moisture (ΔSWC), and vapor pressure deficit (ΔVPD). Carbon uptake anomalies in the prior month ($\Delta\mathrm{NBP}_{-1}$) are also selected to account for autocorrelation. Influences of climate anomalies are indicated by standardized coefficients. Collinearity is assessed using the variance inflation factor (VIF).

Region	Metrics	Intercept	$\Delta\mathrm{NBP}_{-1}$	ΔT	ΔR_{sw}	ΔP	ΔSWC	ΔVPD
Southern Great Plains	lag	-	1	0	-	1	0	1
	coef.	−0.020	0.379	−0.054	-	0.241	−0.032	−0.123
	s.e.	0.008	0.009	0.009	-	0.011	0.010	0.011
	VIF	-	1.098	1.181	-	1.776	1.609	1.820
	SBC	22935.97						
	r	0.549						
Pacific–Mountainous West	lag	-	1	1	0	0	-	0
	coef.	−0.025	0.310	0.158	0.091	−0.099	-	−0.067
	s.e.	0.010	0.010	0.011	0.013	0.013	-	0.013
	VIF	-	1.050	1.209	1.690	1.501	-	1.486
	SBC	17900.52						
	r	0.424						
Central Gulf Coast	lag	-	1	1	0	0	0	0
	coef.	−0.003	0.390	0.212	0.258	−0.230	0.148	−0.361
	s.e.	0.010	0.011	0.012	0.013	0.013	0.013	0.015
	VIF	-	1.071	1.182	1.457	1.452	1.578	1.918
	SBC	13135.04						
	r	0.633						

continued on the next page

Region	Metrics	Intercept	ΔNBP_{-1}	ΔT	ΔR_{sw}	ΔP	ΔSWC	ΔVPD
continued from the previous page								
Upper Midwest	lag	-	1	-	0	0	-	0
	coef.	−0.005	0.397	-	0.047	−0.151	-	0.154
	s.e.	0.009	0.013	-	0.012	0.013	-	0.019
	VIF	-	1.059	-	1.159	1.412	-	1.352
	SBC	9405.35						
	r	0.343						
Northern Rockies	lag	-	1	0	0	0	-	0
	coef.	0.004	0.295	0.062	0.114	−0.114	-	−0.280
	s.e.	0.009	0.011	0.011	0.014	0.012	-	0.015
	VIF	-	1.040	1.487	1.849	1.633	-	2.038
	SBC	17706.19						
	r	0.392						
Southern Appalachia	lag	-	1	-	-	0	0	-
	coef.	−0.001	0.273	-	-	−0.169	0.217	-
	s.e.	0.016	0.020	-	-	0.017	0.018	-
	VIF	-	1.096	-	-	1.115	1.139	-
	SBC	5447.00						
	r	0.525						

Table S9. Explanatory variables with uncertain influences on carbon uptake anomalies: soil moisture anomalies (ΔSWC) for the southern Great Plains, vapor pressure deficit anomalies (ΔVPD) for the Pacific–Mountainous West, shortwave radiation anomalies (ΔR_{sw}) for upper Midwest, and temperature anomalies (ΔT) for northern Rockies. For each region, we identify explanatory variables with uncertain influences (orange columns) by examining standardized coefficients from models that use only a subset of explanatory variables from the selected model (green rows; same models as in Table S8). An explanatory variable has an uncertain influence on carbon uptake anomalies, if its standardized coefficients change sign among these submodels tested. These variables are labeled as empty symbols in Fig. 4a in the main text.

Region	ID	Coefficients					SBC
		ΔNBP_{-1}	ΔT	ΔP_{-1}	ΔSWC	ΔVPD_{-1}	
Southern Great Plains	32	0.379	−0.054	0.241	−0.032	−0.123	22,936
	24	0.383	-	0.243	−0.020	−0.133	22,966
	16	0.404	−0.067	0.294	−0.006	-	23,042
	8	0.411	-	0.302	0.012	-	23,092
	30	0.344	−0.057	-	0.049	−0.229	23,385
	22	0.348	-	-	0.063	−0.240	23,417
	14	0.388	−0.084	-	0.150	-	23,833
	6	0.396	-	-	0.179	-	23,909
	31	-	−0.070	0.153	−0.002	−0.239	24,484
	23	-	-	0.156	0.013	−0.253	24,532
	29	-	−0.072	-	0.046	−0.300	24,636
	21	-	-	-	0.064	−0.315	24,687
	15	-	−0.096	0.261	0.060	-	24,901
	7	-	-	0.272	0.087	-	24,995
	13	-	−0.113	-	0.193	-	25,407
	5	-	-	-	0.232	-	25,530

continued on the next page

continued from the previous page

Region	ID	Coefficients					SBC
		ΔNBP_{-1}	ΔT_{-1}	ΔR_{sw}	ΔP	ΔVPD	
Pacific–Mountainous West	32	0.310	0.158	0.091	−0.099	−0.067	17,901
	28	0.307	0.162	-	−0.144	−0.039	17,939
	30	0.312	0.148	0.147	-	−0.060	17,955
	24	0.313	-	0.103	−0.078	0.002	18,105
	26	0.308	0.149	-	-	0.009	18,113
	22	0.315	-	0.147	-	0.004	18,135
	20	0.310	-	-	−0.129	0.035	18,156
	18	0.312	-	-	-	0.073	18,294
	31	-	0.173	0.079	−0.110	−0.009	18,746
	27	-	0.177	-	−0.149	0.015	18,769
	29	-	0.163	0.141	-	−0.002	18,807
	25	-	0.164	-	-	0.064	18,937
	23	-	-	0.093	−0.088	0.064	18,962
	19	-	-	-	−0.134	0.094	18,997
	21	-	-	0.143	-	0.066	18,999
	17	-	-	-	-	0.133	19,132
		ΔNBP_{-1}		ΔR_{sw}	ΔP	ΔVPD	
Upper Midwest	16	0.397		0.047	−0.151	0.154	9405
	8	0.405		0.039	−0.206	-	9460
	14	0.399		0.087	-	0.242	9530
	6	0.433		0.101	-	-	9715
	15	-		−0.019	−0.200	0.186	10,188
	7	-		−0.027	−0.268	-	10,243
	13	-		0.029	-	0.332	10,349
	5	-		0.058	-	-	10,601

continued on the next page

Region	ID	Coefficients					SBC
continued from the previous page							
		ΔNBP_{-1}	ΔT	ΔR_{sw}	ΔP	ΔVPD	
Northern Rockies	32	0.295	0.062	0.114	−0.114	−0.280	17,706
	28	0.301	0.053	-	−0.163	−0.235	17,766
	30	0.286	0.069	0.174	-	−0.260	17,783
	26	0.291	0.056	-	-	−0.149	17,975
	12	0.278	−0.033	-	−0.095	-	18,006
	16	0.275	−0.035	0.026	−0.081	-	18,010
	14	0.270	−0.025	0.070	-	-	18,044
	10	0.277	−0.010	-	-	-	18,082
	31	-	0.060	0.131	−0.088	−0.218	18,378
	29	-	0.067	0.178	-	−0.206	18,417
	27	-	0.047	-	−0.143	−0.160	18,453
	15	-	−0.019	0.054	−0.068	-	18,545
	11	-	−0.014	-	−0.098	-	18,555
	13	-	−0.010	0.092	-	-	18,565
	25	-	0.049	-	-	−0.086	18,604
	9	-	0.009	-	-	-	18,633

Table S10. Attribution of carbon uptake anomalies in early (December–May) and late seasons (June–November) for selected ENSO-sensitive regions. Also shown are coefficients from a test for upper Midwest without using the data from 2012, an exceptional drought year.

Region	Period	Metrics	Intercept	ΔNBP_{-1}	ΔT	ΔR_{sw}	ΔP	ΔSWC	ΔVPD
Upper Midwest	Without 2012	lag	-	1	-	-	0	-	0
		coef.	−0.047	0.341	-	-	−0.174	-	0.141
		s.e.	0.010	0.014	-	-	0.014	-	0.016
		SBC				8200.44			
		r				0.399			
	Winter & Spring	lag	-	1	-	0	0	-	0
		coef.	−0.009	0.183	-	0.036	−0.074	-	0.182
		s.e.	0.010	0.012	-	0.011	0.013	-	0.012
		SBC				2514.35			
		r				0.615			
	Summer & Fall	lag	-	1	0	-	0	0	1
		coef.	−0.015	0.469	−0.175	-	−0.449	−0.100	−0.295
		s.e.	0.022	0.025	0.027	-	0.029	0.027	0.045
		SBC				6153.40			
		r				0.535			
Northern Rockies	Winter & Spring	lag	-	1	0	-	0	0	1
		coef.	0.011	0.184	0.039	-	−0.064	0.072	0.148
		s.e.	0.010	0.010	0.010	-	0.010	0.011	0.011
		SBC				6043.65			
		r				0.409			
	Summer & Fall	lag	-	1	-	0	0	-	0
		coef.	0.003	0.403	-	0.322	−0.175	-	−0.541
		s.e.	0.016	0.018	-	0.028	0.024	-	0.023
		SBC				10573.28			
		r				0.444			
Southern Appalachia	Winter & Spring	lag	-	1	-	2	0	0	0
		coef.	−0.040	0.238	-	−0.119	−0.123	0.220	0.094
		s.e.	0.016	0.019	-	0.018	0.018	0.019	0.020
		SBC				1897.18			
		r				0.618			
	Summer & Fall	lag	-	1	0	0	1	-	-
		coef.	0.034	0.420	−0.273	0.116	0.236	-	-
		s.e.	0.029	0.039	0.031	0.029	0.030	-	-
		SBC				3210.85			
		r				0.573			

Table S11. Summary of regressions for evaluating PNA and NAO influences on net carbon uptake anomalies integrated over North America (ΔNBP). All regressions have a constant term (i.e., intercept). The inclusion of the PNA or NAO index in the regression actually degrades model performance according to the Schwarz Bayesian information criterion (SBC).

	$\Delta\text{NBP} \sim \text{ONI}$	$\Delta\text{NBP} \sim \text{ONI} + \text{PNA}$	$\Delta\text{NBP} \sim \text{ONI} + \text{NAO}$
R^2	0.045	0.065	0.049
Adj. R^2	0.036	0.047	0.031
SBC	1264.3	1266.6	1268.5
D.f. model[1]	1	2	2
$\hat{\beta}_{\text{ONI}}$	18.846	17.702	18.688
p_{ONI}	0.028	0.039	0.030
$\hat{\beta}_{\text{PNA}}$	n/a	12.955	n/a
p_{PNA}	n/a	0.133	n/a
$\hat{\beta}_{\text{NAO}}$	n/a	n/a	−4.547
p_{NAO}	n/a	n/a	0.507

[1]Degree of freedom of the model.

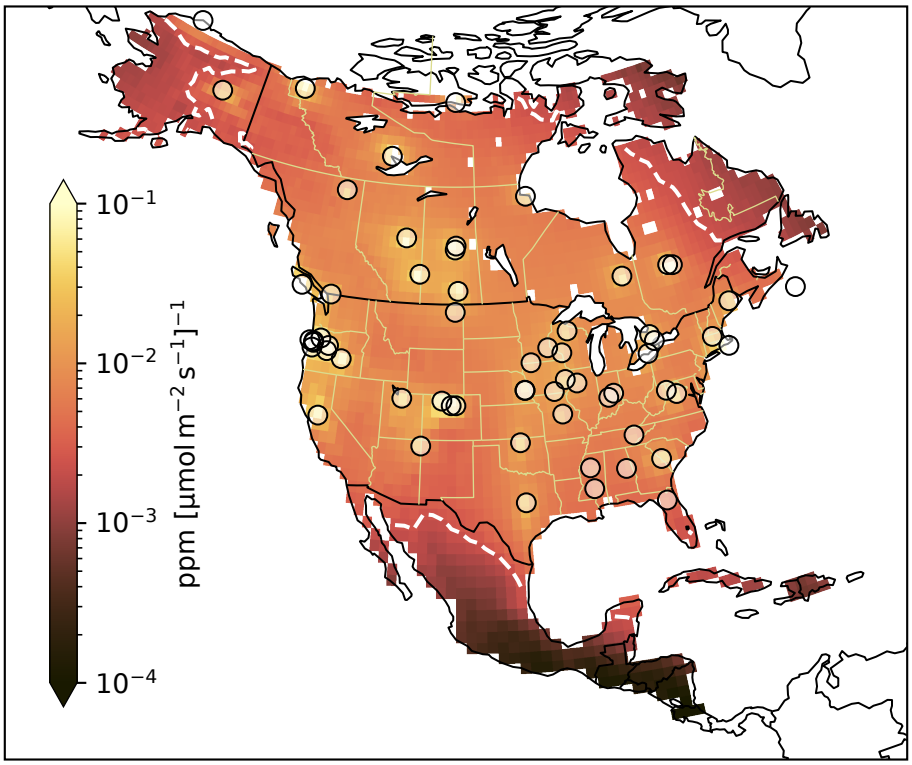

Fig. S1. Mean sensitivity of atmospheric CO_2 concentration observations to surface net CO_2 fluxes (ppm [μmol m^{-2} s^{-1}]$^{-1}$) over North America, averaged over 2007–2015. Translucent circles indicate continuous CO_2 monitoring sites (Table S1). Grid cells enclosed within the dashed white contours are those for which the sensitivity of CO_2 observations to surface fluxes is among the top 80 % over North America.

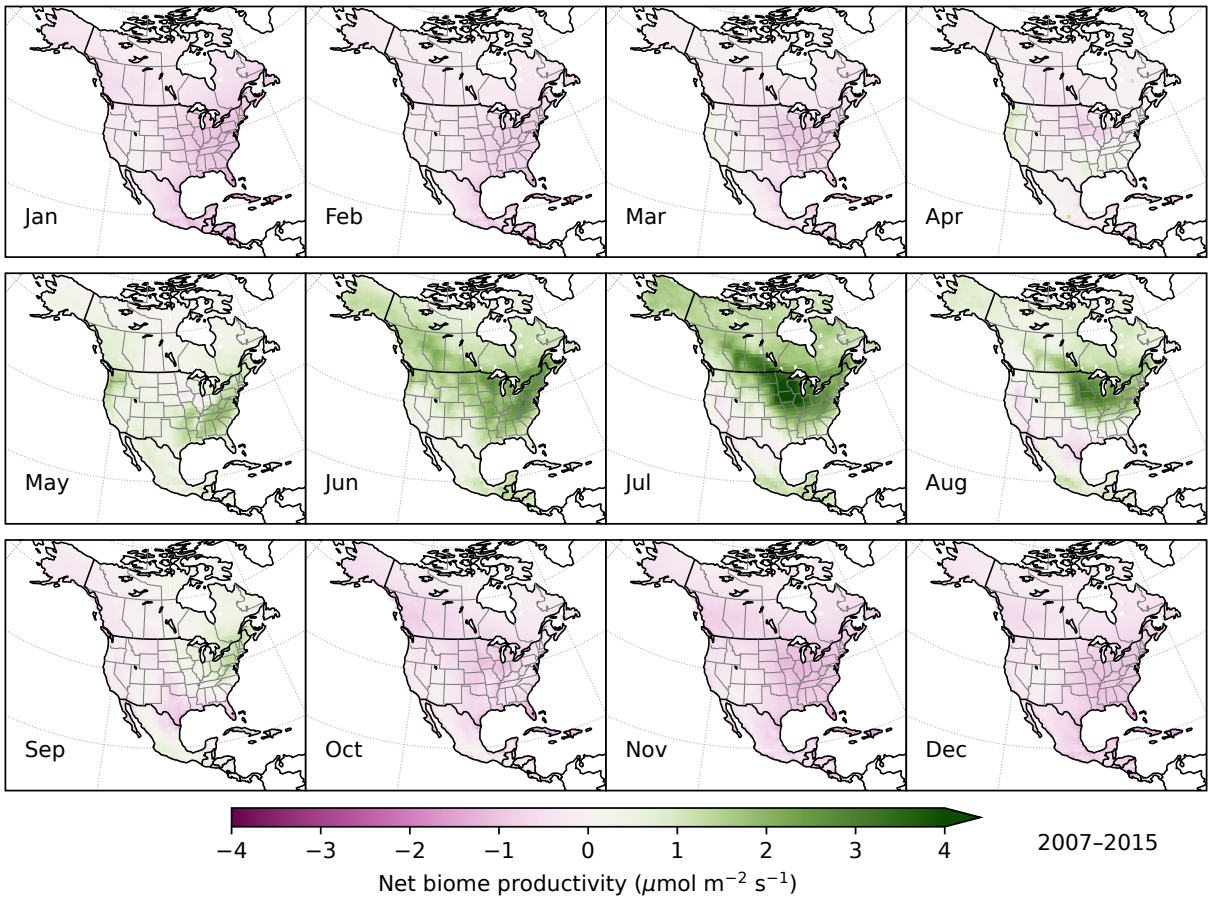

Fig. S2. Multi-year (2007–2015) mean monthly patterns of geostatistical inverse estimates of net biome productivity (NBP) over North America.

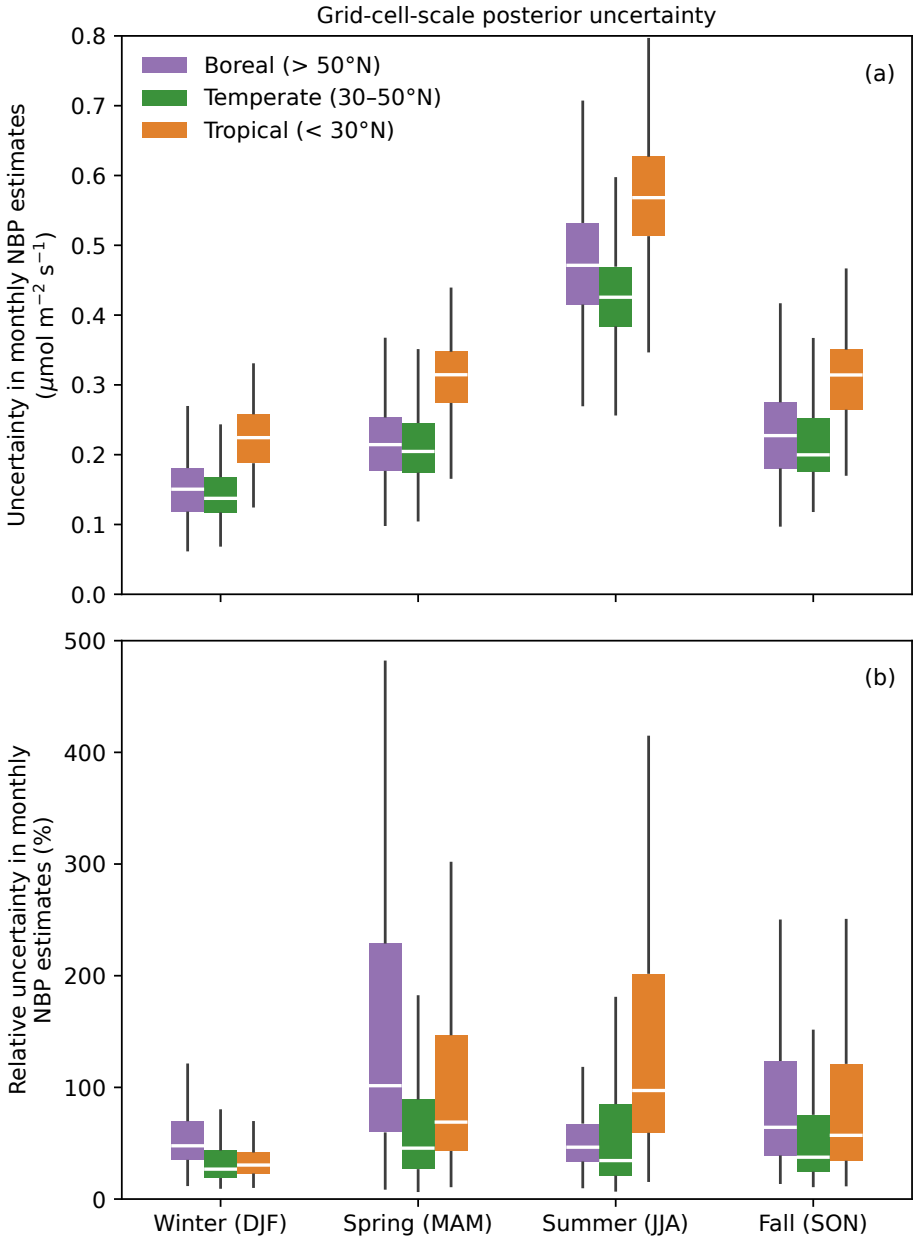

Fig. S3. A summary of the grid-cell-scale posterior uncertainties in monthly carbon uptake (NBP) estimates, grouped by season and latitudinal band. (**a**) Boxplot of the grid-cell-scale posterior uncertainties in monthly NBP estimates, with the center bar, bounds of box, and whiskers representing the median, first and third quartiles, smallest and largest anomalies falling within 1.5× of the interquartile range from the nearest quartiles. (**b**) Similar to (**a**) but for grid-cell-scale relative posterior uncertainties. Note that it is typical for grid cells with near-neutral carbon flux estimates to show large relative uncertainties. NBP estimates in the temperate zone are generally associated with lower uncertainties and relative uncertainties than in tropical and boreal zones due to stronger observational constraint (Fig. S1).

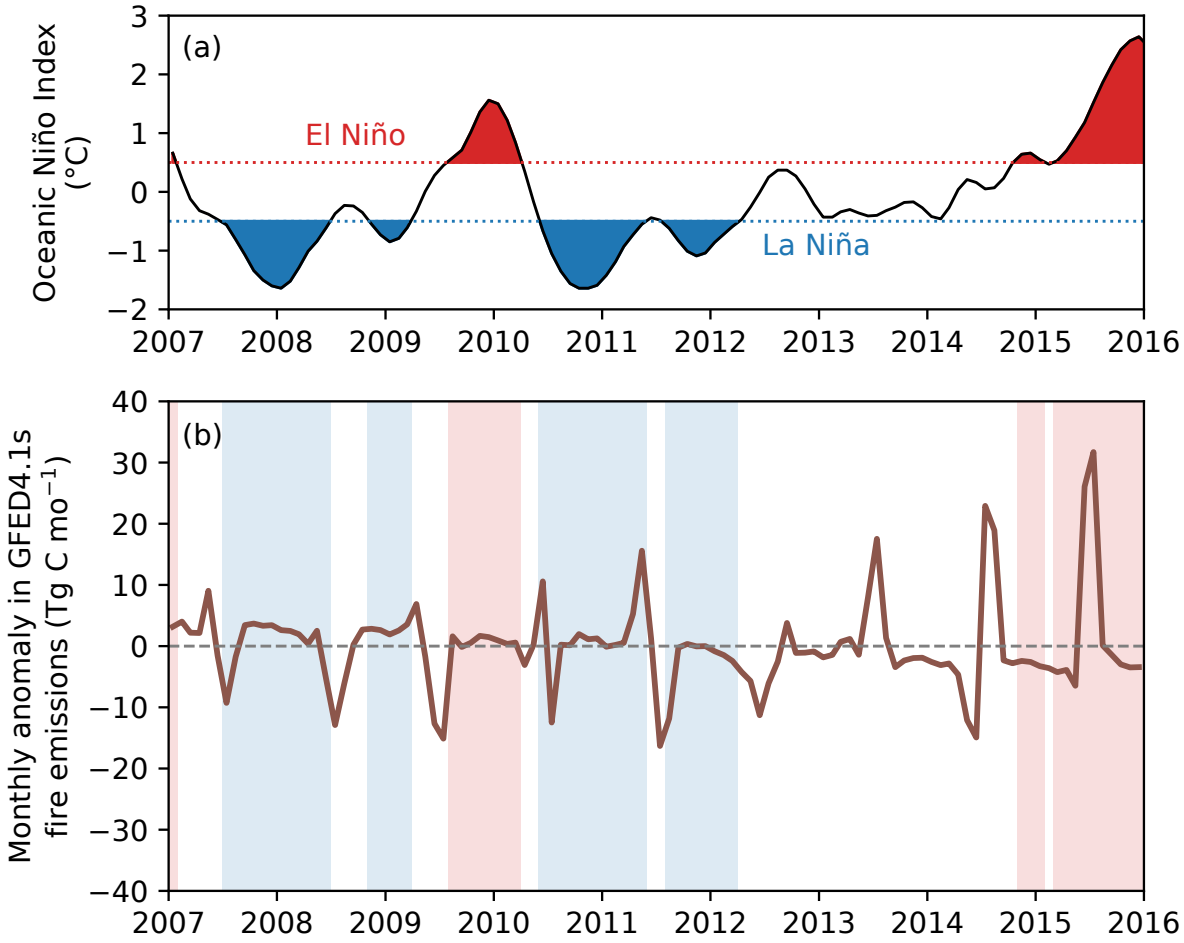

Fig. S4. Detrended anomalies in fire emissions from the Global Fire Emissions Database version 4.1 with small fires (GFED4.1s; van der Werf et al., 2017), presented in the same style as Fig. 2 in the main text. (**a**) Monthly Oceanic Niño Index (ONI). (**b**) Monthly detrended anomalies in fire emissions over North America from GFED4.1s. A positive (negative) anomaly indicates higher (lower) fire emissions relative to the detrended mean seasonal cycle. El Niño and La Niña periods are shaded in light red and light blue, respectively. There is no correlation between monthly fire emission anomaly and the ONI ($r = -0.003$, $p = 0.973$).

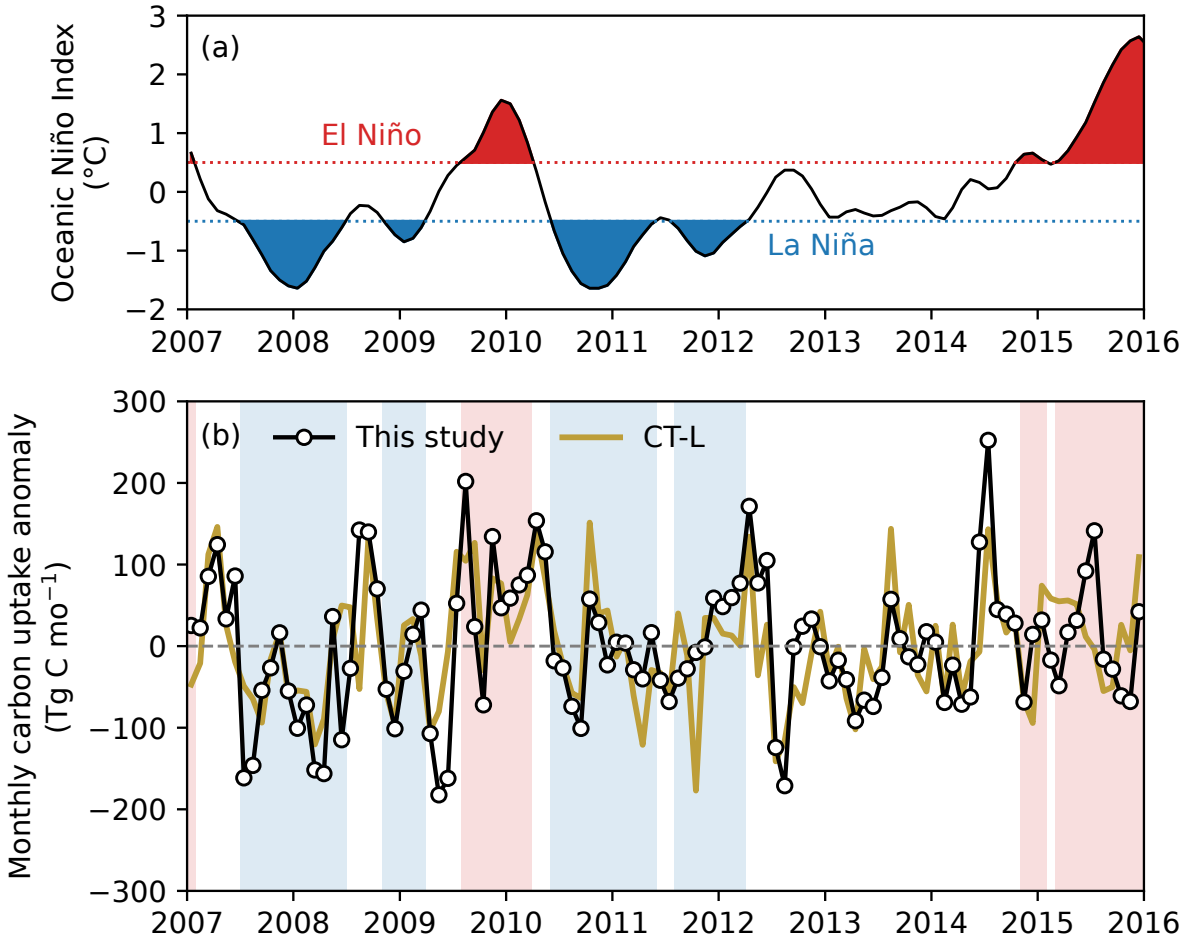

Fig. S5. Comparison of carbon uptake anomalies between geostatistical inverse estimates (this study) and CarbonTracker-Lagrange (CT-L) inverse estimates (Hu et al., 2019), similar to Fig. 2 in the main text. (**a**) Monthly Oceanic Niño Index. (**b**) Monthly anomalies in net biome carbon uptake over North America from geostatistical inverse estimates (empty circles and black line) and from CT-L inverse estimates (dark gold line). A positive (negative) anomaly indicates enhanced (suppressed) carbon uptake by the biosphere. El Niño and La Niña periods are shaded in light red and light blue, respectively.

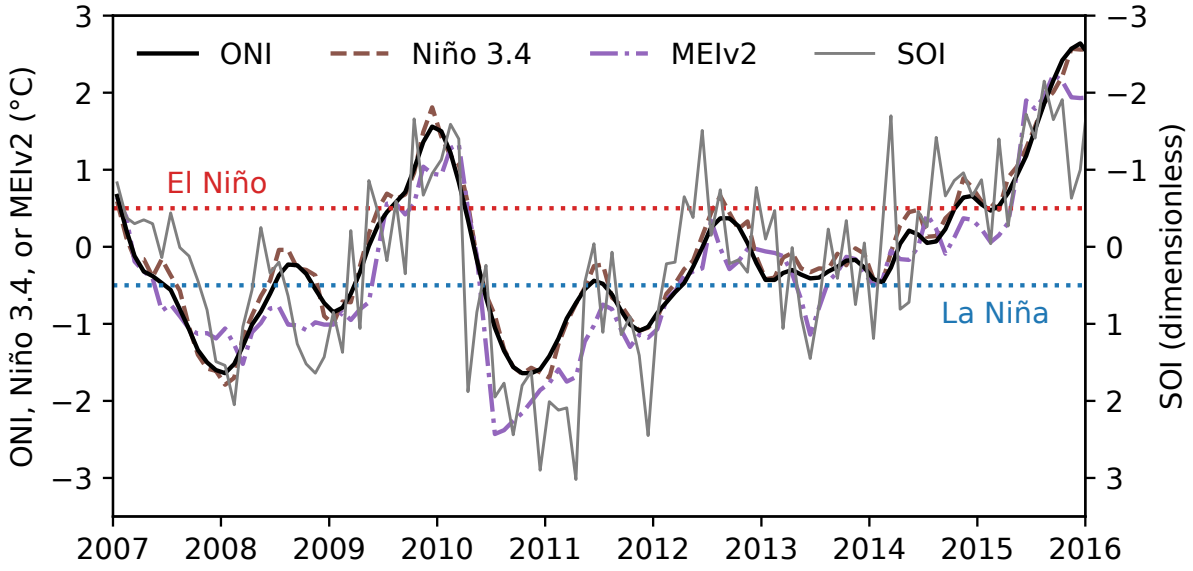

Fig. S6. Time series of the Oceanic Niño Index (ONI, black line), Niño 3.4 Index (brown dashed line), Multivariate ENSO Index version 2 (MEI v2, purple dash-dotted line), and Southern Oscillation Index (SOI, thin gray line) over 2007–2015. Note that SOI values (right vertical axis) are reversed to align with other ENSO indices. Also shown are the thresholds for El Niño and La Niña events in blue and red dotted lines, respectively.

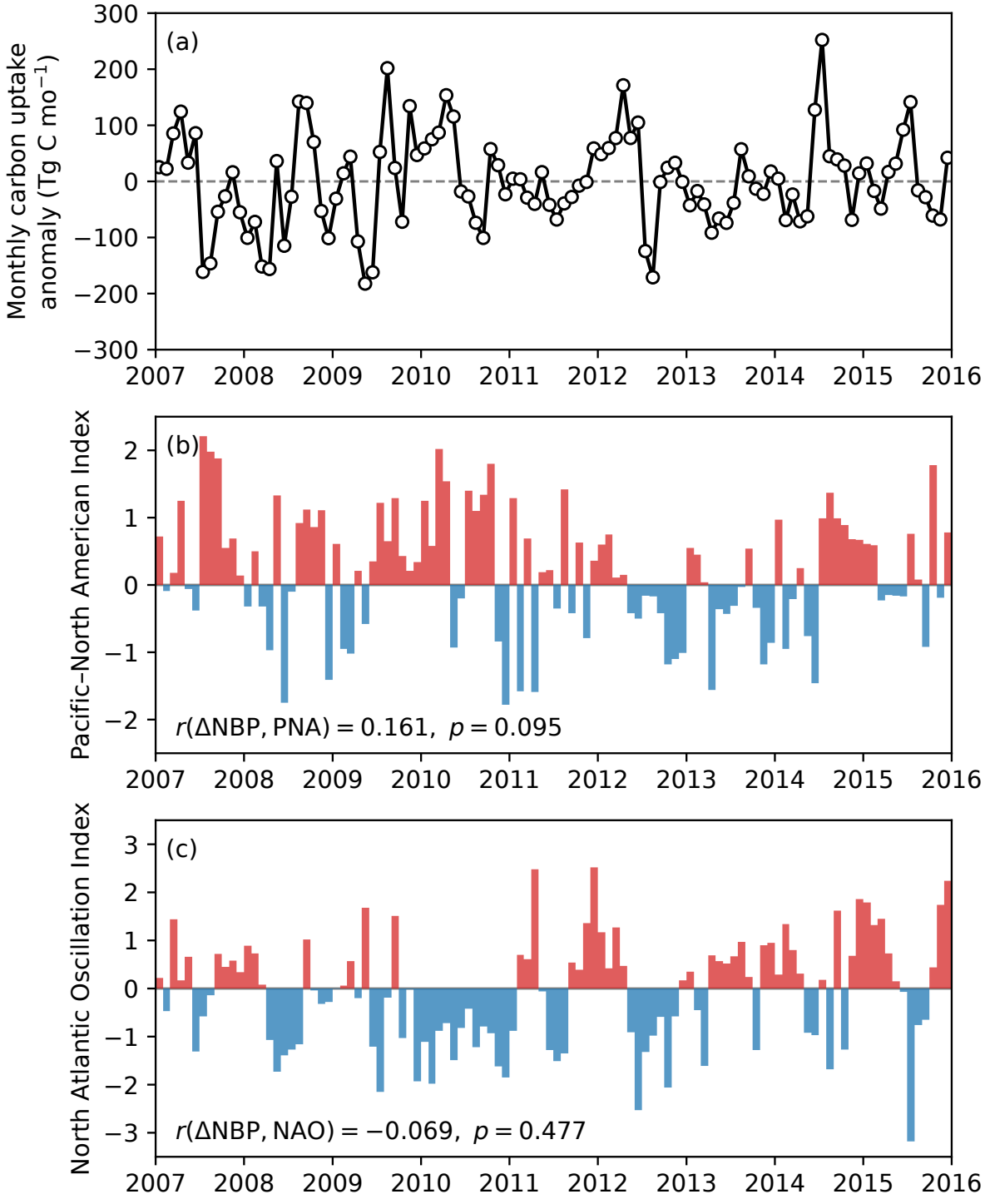

Fig. S7. Monthly time series of (**a**) carbon uptake (NBP) anomalies based on geostatistical inverse estimates (this study), (**b**) the Pacific–North American (PNA) pattern index, and (**c**) the North Atlantic Oscillation (NAO) index during 2007–2015. Also shown are the correlation between NBP anomalies and the PNA index and that between NBP anomalies and the NAO index.

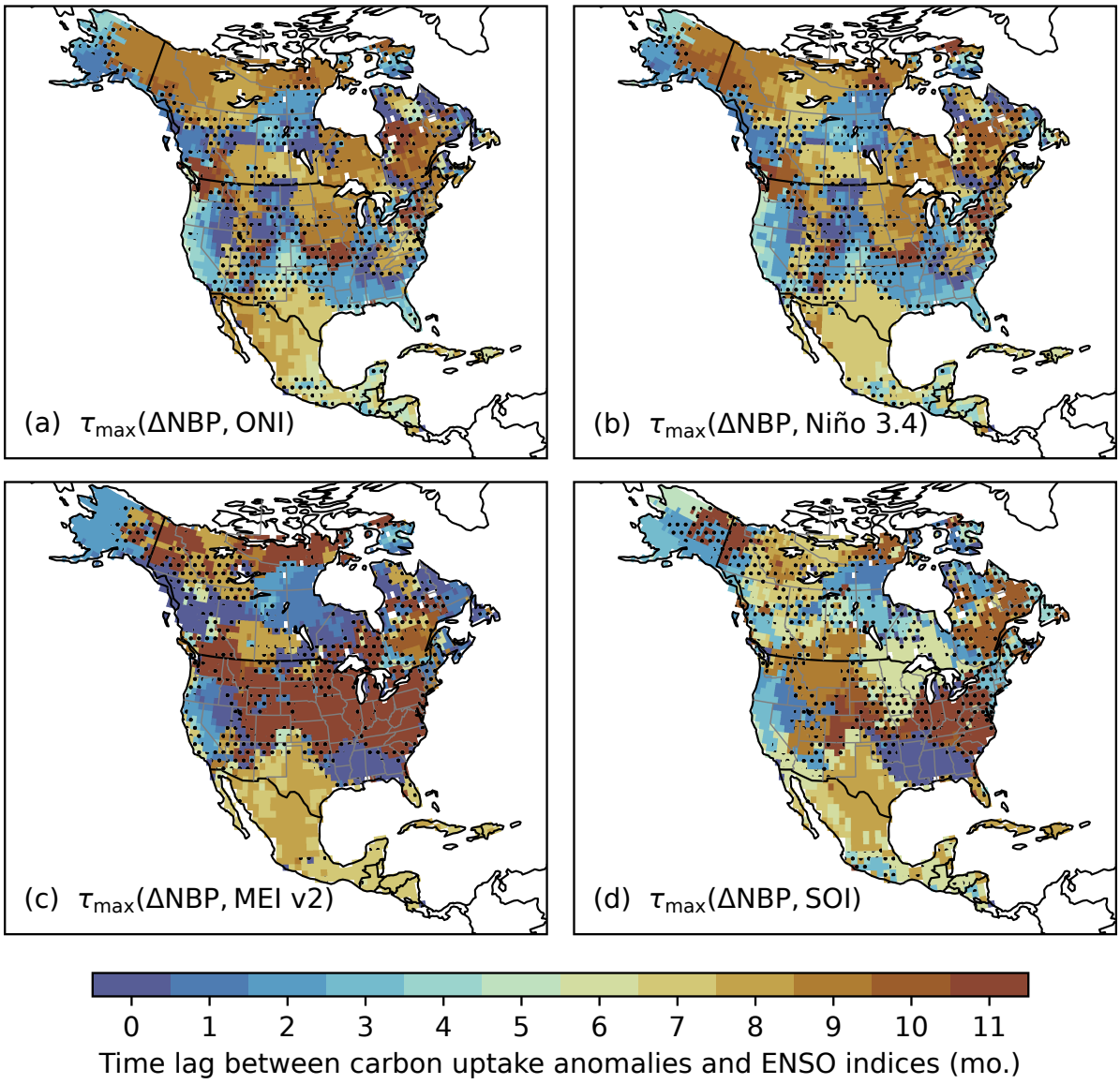

Fig. S8. Time lags of anomalies in net biome productivity (ΔNBP) relative to the Oceanic Niño Index (ONI, **a**), Niño 3.4 Index (**b**), Multivariate ENSO Index version 2 (MEI v2, **c**), and Southern Oscillation Index (SOI, **d**), in months. Time lags are calculated by maximizing the absolute values of cross correlation coefficients. Stippled areas are where time lags are not robustly specified, i.e., when the time lag envelope for $\Delta r = 0.05$ deviation from the maximum absolute correlation is wider than four months (see Sect. 2.7 in the main text).

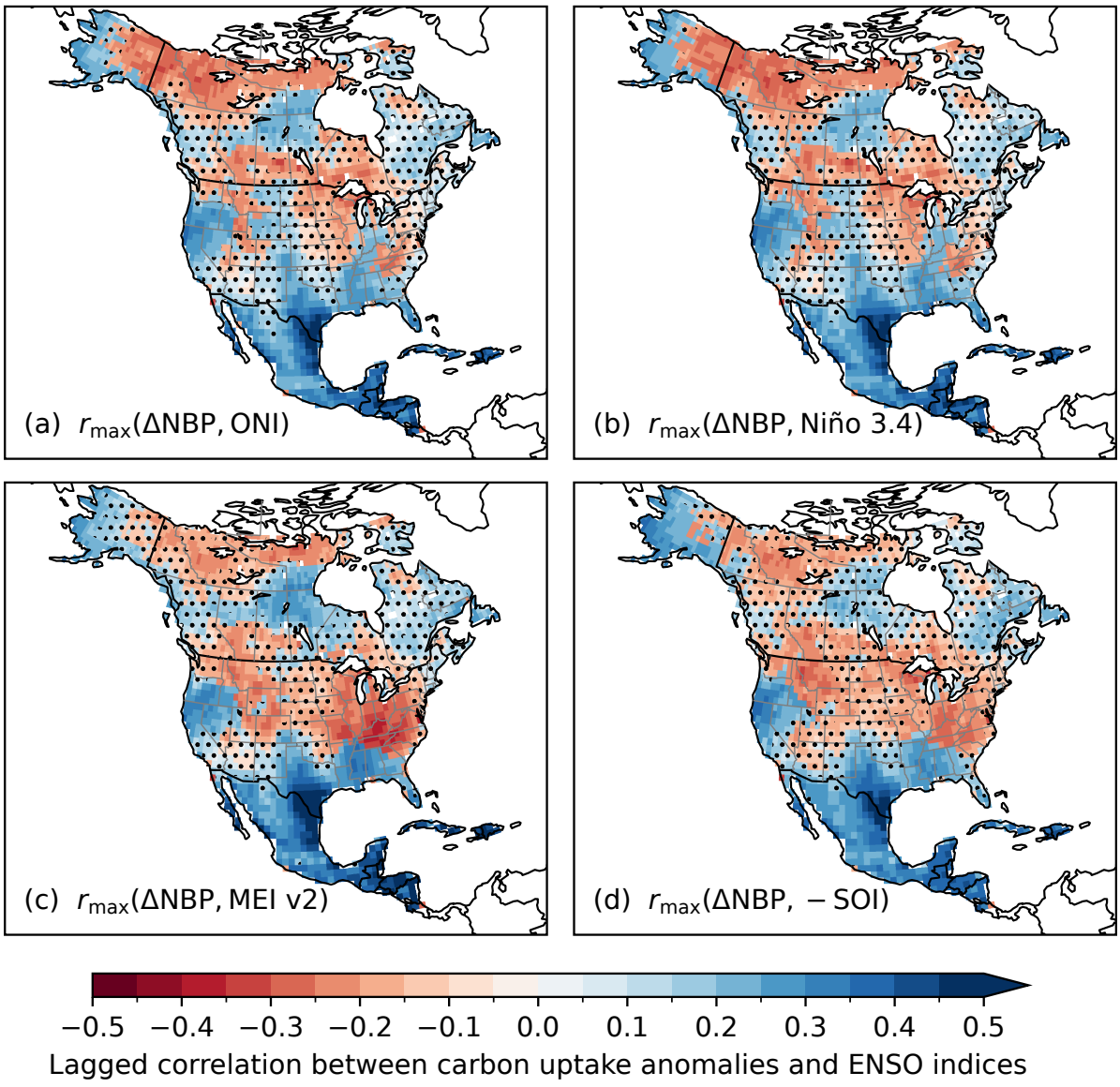

Fig. S9. Lagged Pearson correlations between anomalies in net biome productivity (ΔNBP) and the Oceanic Niño Index (ONI, **a**), Niño 3.4 Index (**b**), Multivariate ENSO Index version 2 (MEI v2, **c**), and the reversed Southern Oscillation Index (SOI, **d**), with the same time lags for each index shown in Fig. S8 considered. Note that the sign of the SOI is reversed to produce a correlation pattern (**d**) that aligns with those for other ENSO indices, due to the negative correlations between the SOI and other ENSO indices used here (see Fig. S6). Values that are *not* statistically significant at $p = 0.05$ level are stippled.

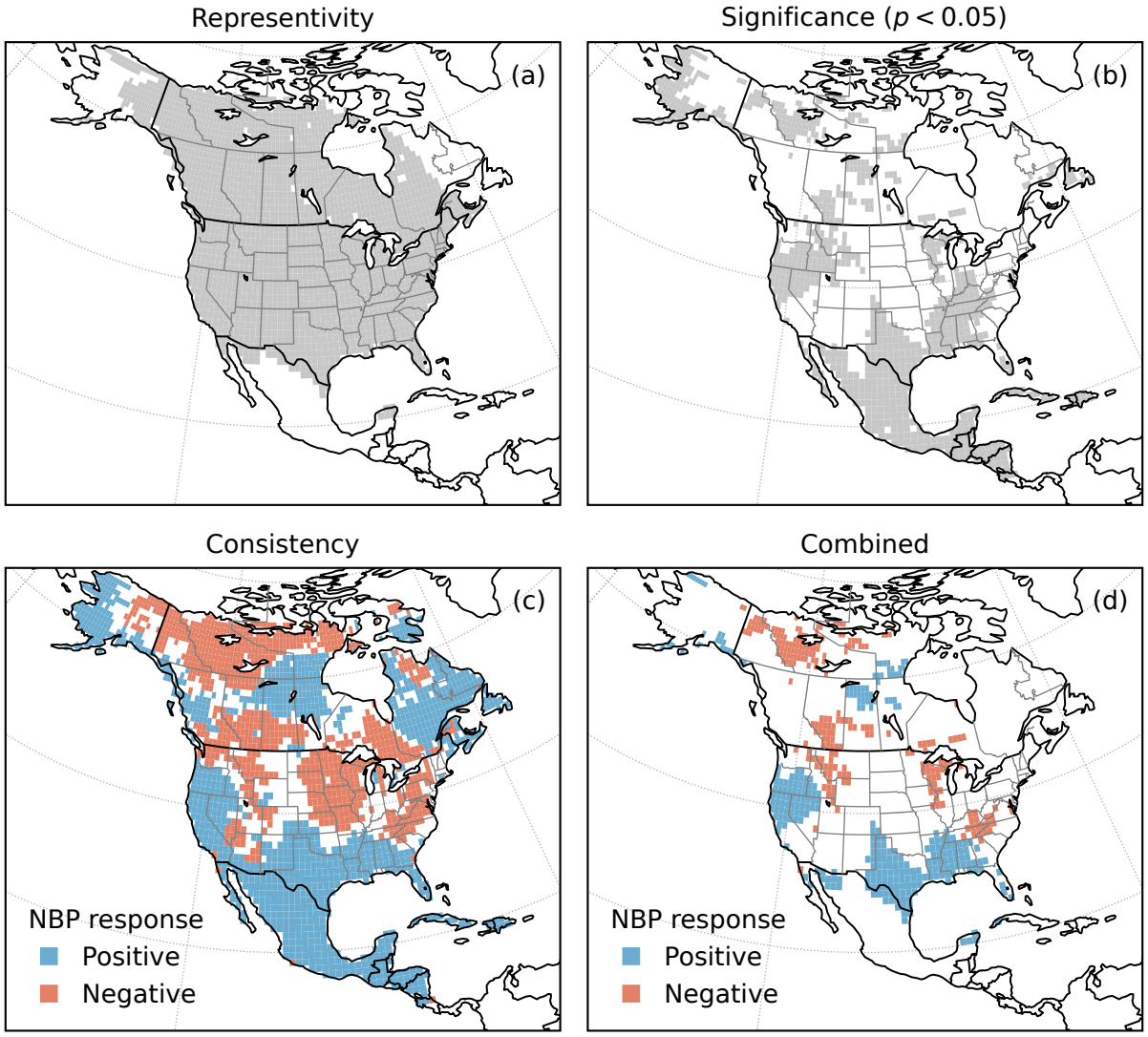

Fig. S10. Masks for identifying ENSO-sensitive regions. (**a**) Representivity mask, defined as the area (gray) for which the sensitivity of CO_2 concentration observations to surface fluxes is among the top 80 % over North America (see Fig. S1). (**b**) Significance mask, defined as the area (gray) for which lagged correlations between carbon uptake anomalies and four ENSO indices (Fig. S9) are all significant at $p < 0.05$ level. (**c**) Consistency mask, defined as the area (red and blue) for which lagged correlations between carbon uptake anomalies and four ENSO indices have consistent signs (Fig. S9), with grid cells showing a positive NBP response to ENSO (i.e., enhanced NBP during El Niño) colored blue and those showing a negative response colored red. (**d**) Combined mask, defined as grid cells that pass representivity, significance, and consistency criteria, with the same color codes as (**c**).

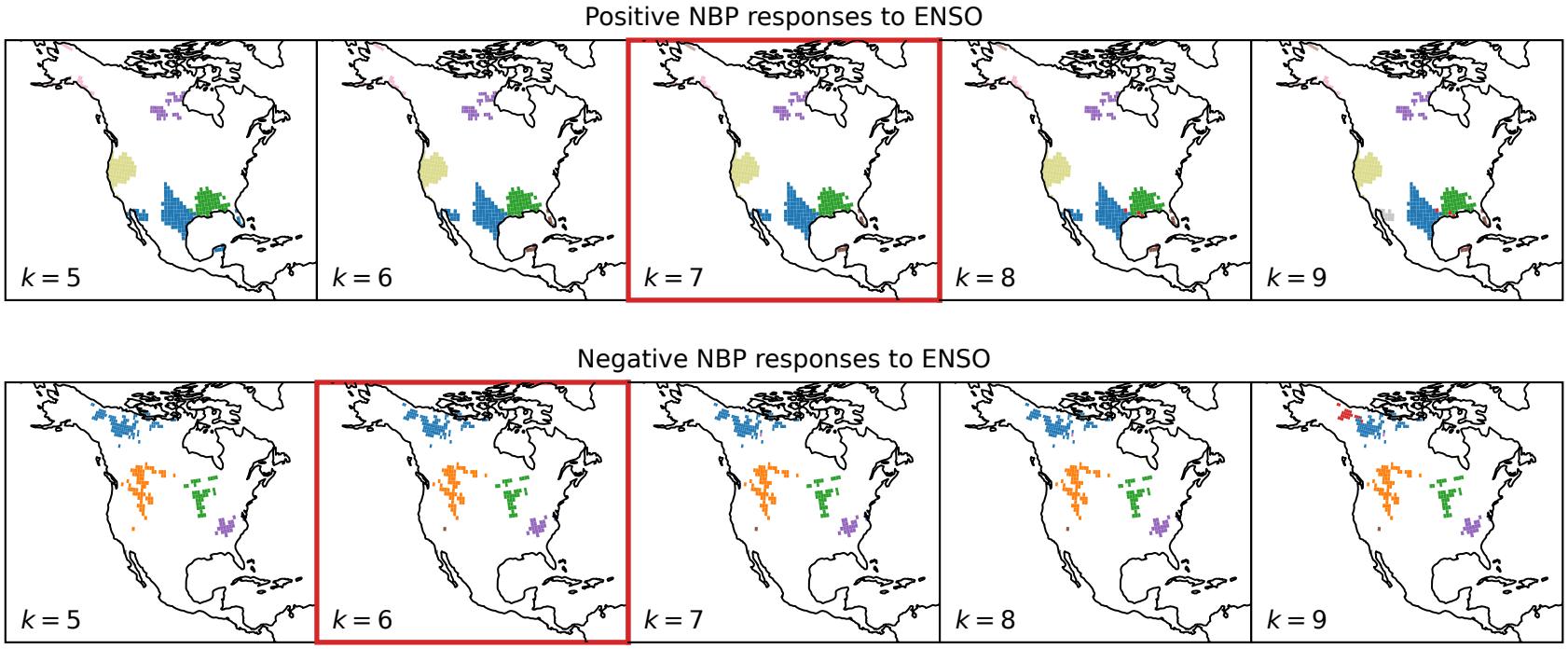

Fig. S11. Test of the number of ENSO-sensitive clusters. Grid cells with positive responses of carbon uptake (NBP) to ENSO (i.e., enhanced NBP during El Niño; top row) are clustered separately from those with negative responses (bottom row). The number of clusters (k) tested are from 5 to 9, and those with the most parsimonious assemblage of clusters are used in the final results (marked in red).

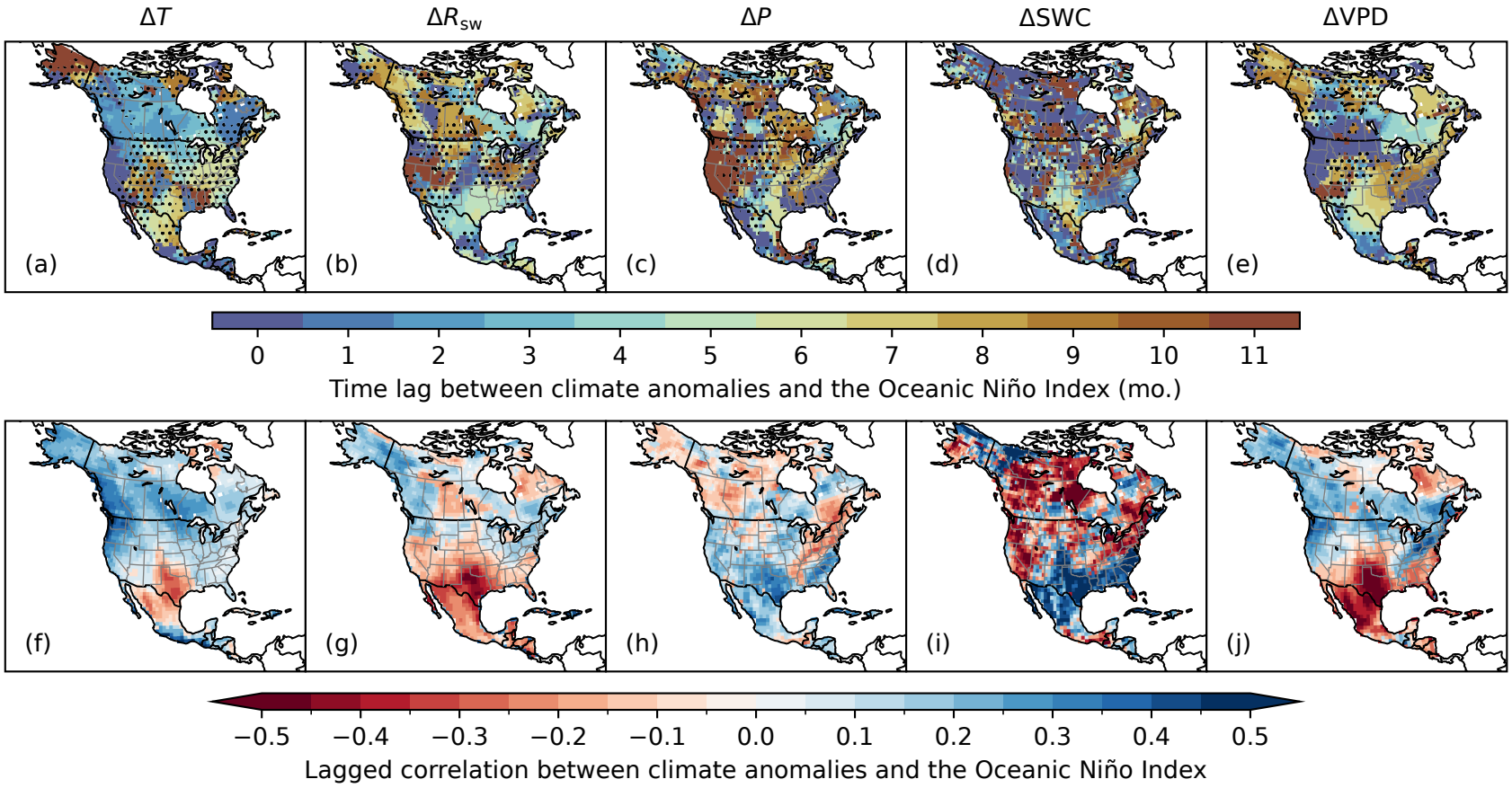

Fig. S12. Time lags of anomalies in surface air temperature (ΔT, **a**), shortwave radiation (ΔR_{sw}, **b**), precipitation (ΔP, **c**), soil water content (ΔSWC, **d**), and vapor pressure deficit (ΔVPD, **e**) relative to the Oceanic Niño Index, in months. Time lags are calculated by maximizing the absolute values of cross correlation coefficients. Similar to Fig. S8, stippled areas are where time lags are not robustly specified, i.e., when the time lag envelope for $\Delta r = 0.05$ deviation from the maximum absolute correlation is wider than four months (see Methods in the main text). Also shown are lagged Pearson correlations between climate anomalies and the Oceanic Niño Index (**f**–**j**), with the same time lags corresponding to each climate variable (**a**–**e**) considered.

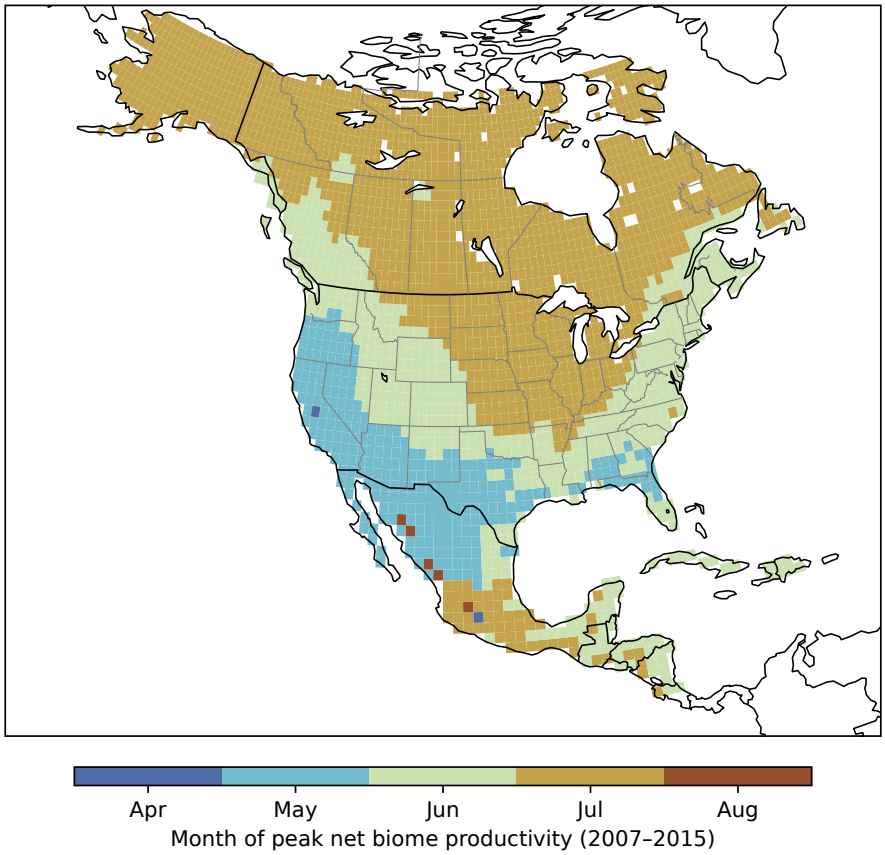

Fig. S13. Spatial pattern of the month of peak net biome productivity, identified from the multi-year (2007–2015) mean seasonal cycle at each grid cell.

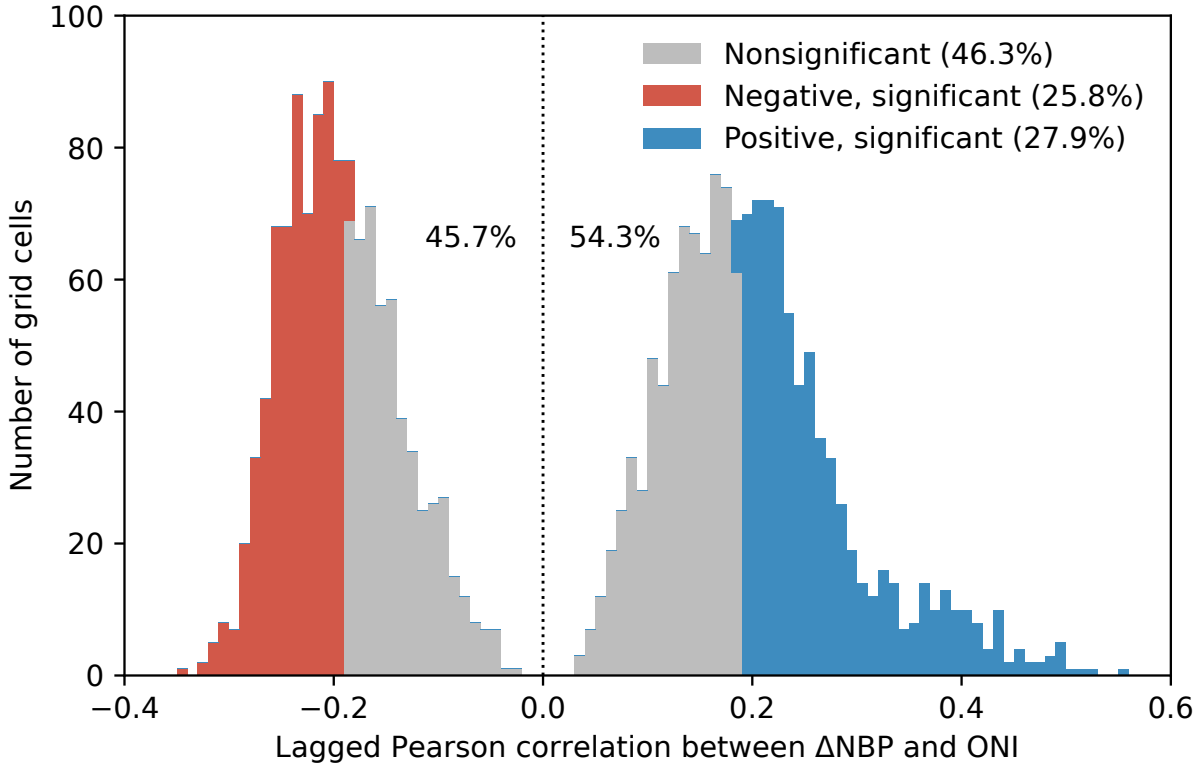

Fig. S14. Histogram of lagged Pearson correlations between carbon uptake anomalies (ΔNBP) and the Oceanic Niño Index (ONI). The majority of grid cells (54.3 %) and area (59.6 %) show a positive correlation between carbon uptake anomalies and the ONI (right side of the vertical dashed line). 27.9 % (25.8 %) of all grid cells, which occupy 32.2 % (20.6 %) of the total area of North America, show a statistically significant ($p < 0.05$) positive (negative) correlation between ΔNBP and ONI.

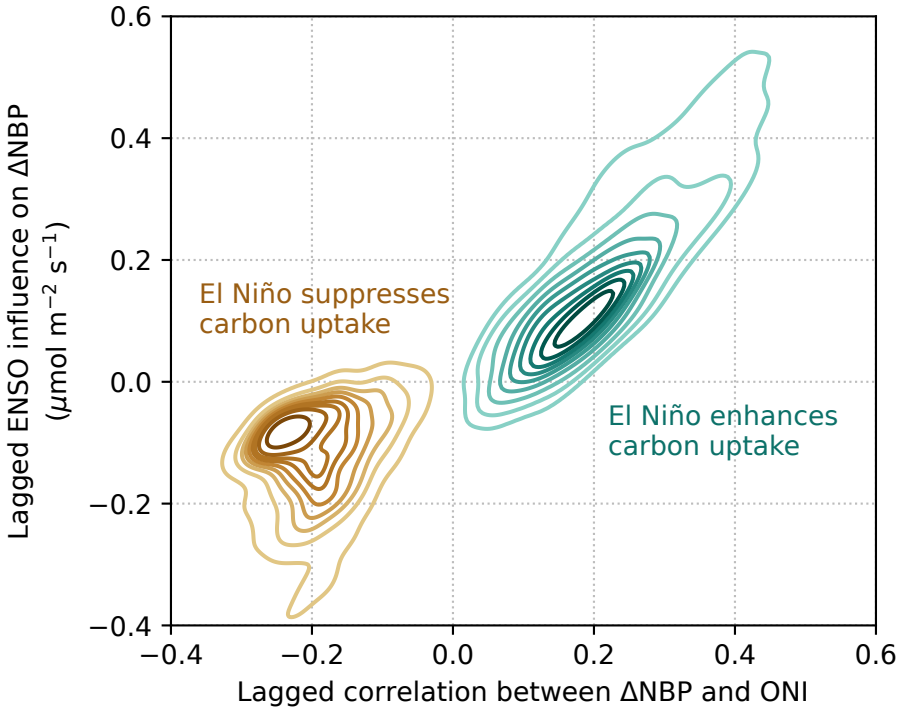

Fig. S15. Across grid cells, El Niño enhancement of carbon uptake (turquoise) dominates its suppression of carbon uptake (brown). Values on the horizontal axis correspond to the lagged correlations shown in Fig. 1b in the main text, whereas those on the vertical axis correspond to ENSO composite influences (El Niño − La Niña) on carbon uptake anomalies (ΔNBP) shown in Fig. 1c in the main text. Contours represent the first decile (0–10 %) to the ninth decile (80–90 %) of the statistical distribution based on 2-D kernel density estimation. The "enhancement" cluster (turquoise) shows disproportionately larger ENSO influence on ΔNBP in than the "suppression" cluster (brown), giving rise to the aggregated North American response: El Niño enhances the North American land carbon sink.

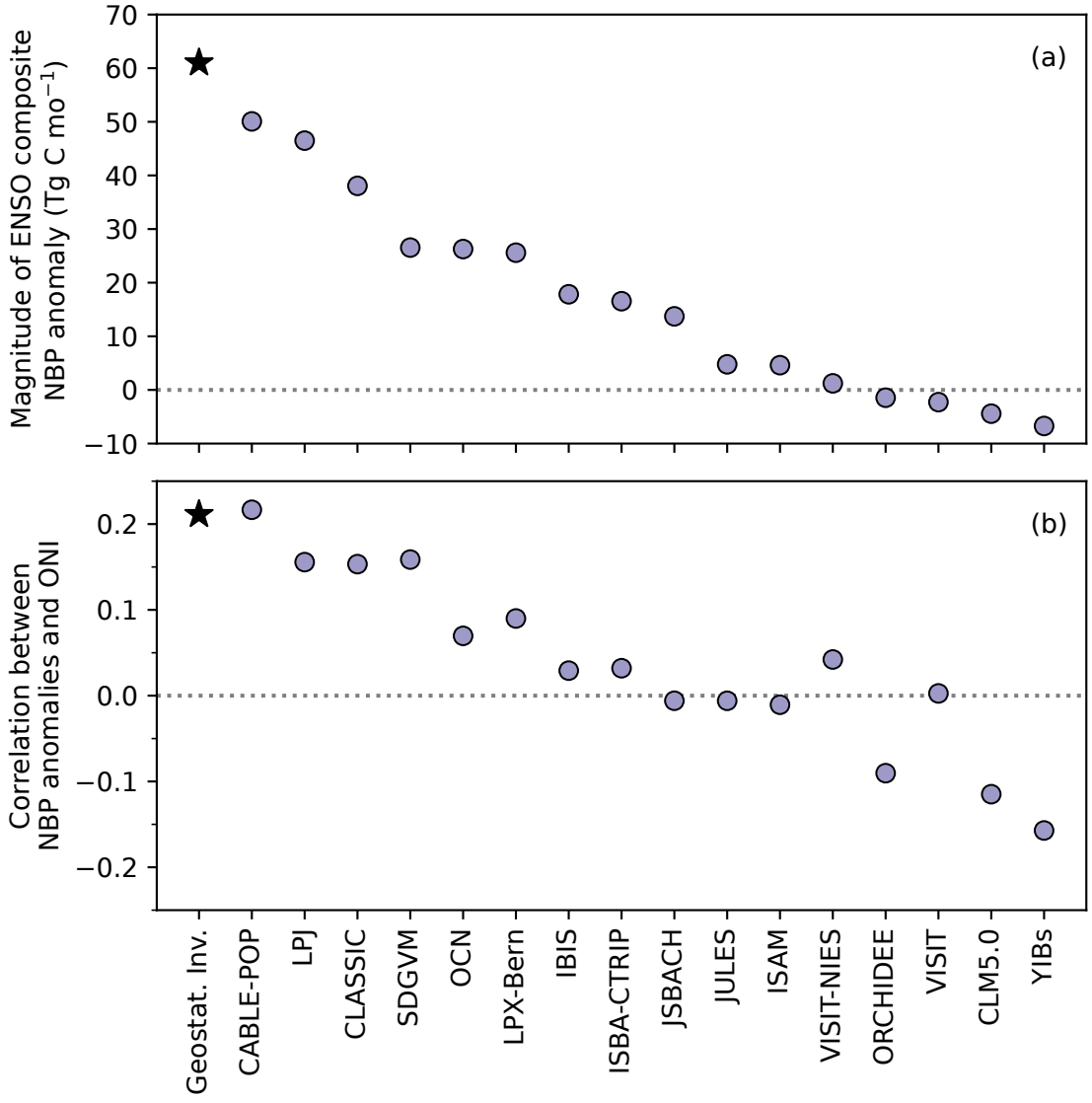

Fig. S16. Comparison of ENSO impact on North American aggregated carbon uptake (NBP) between geostatistical inverse estimates (this study) and members of the TRENDY v11 model ensemble (Friedlingstein et al., 2022; Sitch et al., 2024). (**a**) Magnitudes of ENSO composite differences (El Niño − La Niña) in aggregated North American NBP anomalies during 2007–2015, for the geostatistical inversion (star) and TRENDY models (circles). Models are ranked in descending order by the ENSO composite anomaly. A small subset of TRENDY models show the opposite sign of ENSO impact (i.e., negative NBP anomaly during El Niño). (**b**) Correlations between monthly North American aggregated NBP anomalies and the Oceanic Niño Index (ONI) across the same set of models (following the same order as in **a**).

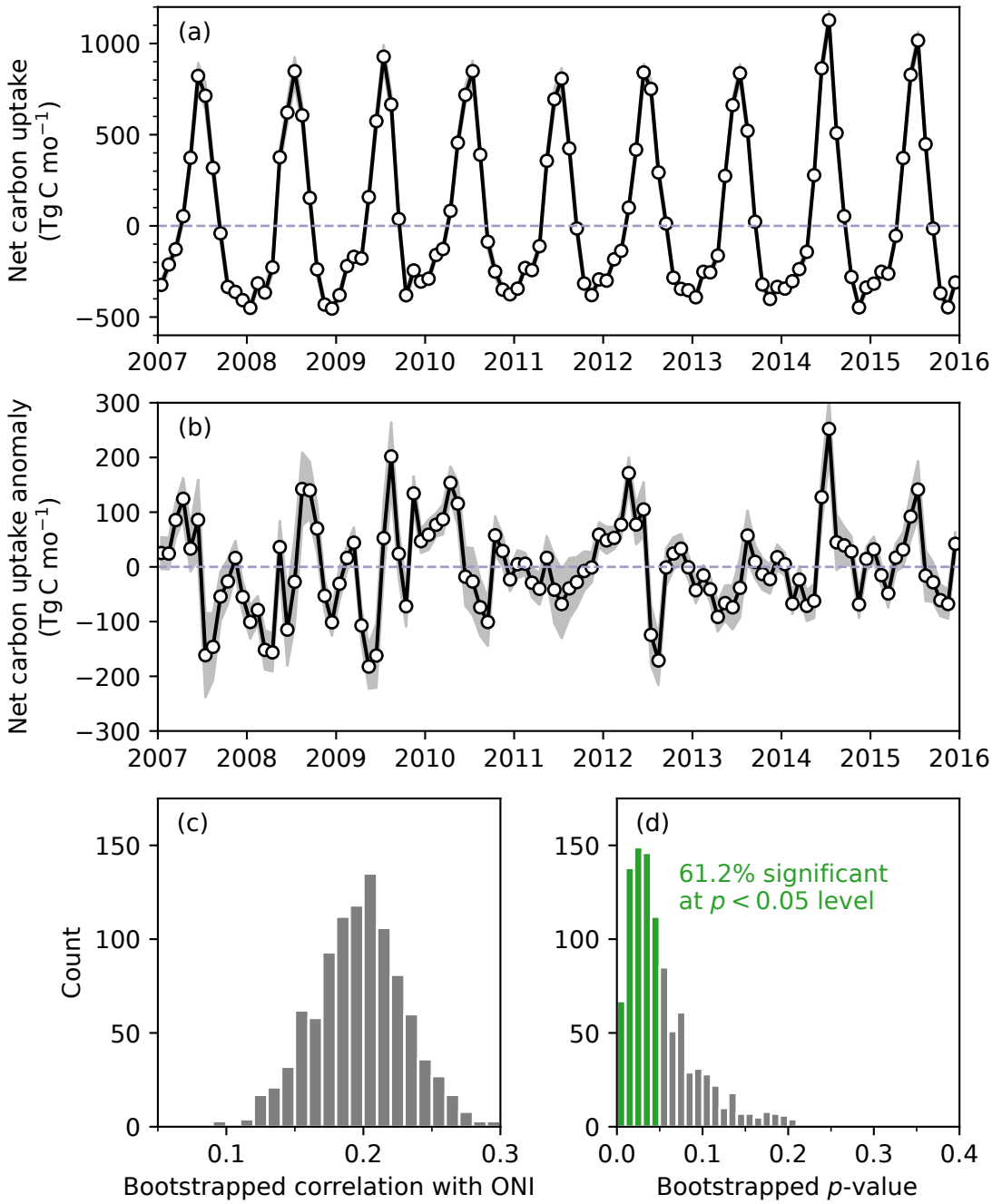

Fig. S17. Posterior uncertainty in net biome carbon uptake anomalies over North America and its implications for the robustness of ENSO impact. (**a**) Monthly net biome carbon uptake aggregated over North America, with $\pm 1\,\sigma$ uncertainty shown in gray shading. (**b**) Similiar to (**a**) but for deseasonalized anomalies in North American net biome carbon uptake, with $\pm 1\,\sigma$ uncertainty in gray. (**c** and **d**) Statistical distributions of the correlation between carbon uptake anomalies and the Oceanic Niño Index (ONI) and the associated p-value based on bootstrapping the uncertainty range of flux estimates for $N = 1000$ times.

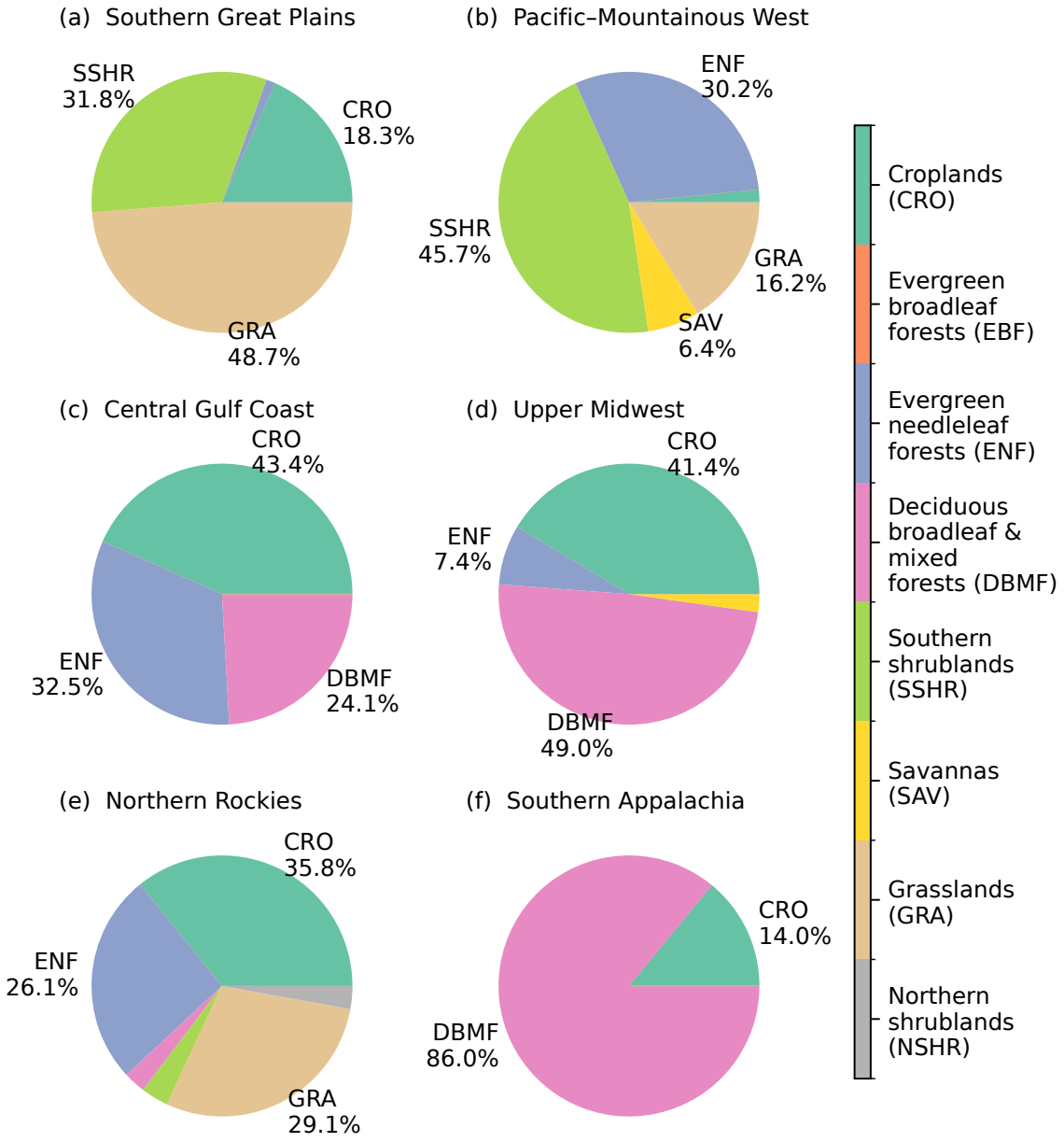

Fig. S18. Pie charts of biome areal fractions in each identified ENSO-sensitive region in temperate North America. Biomes that cover more than 5 % of a region are labeled in pie charts.

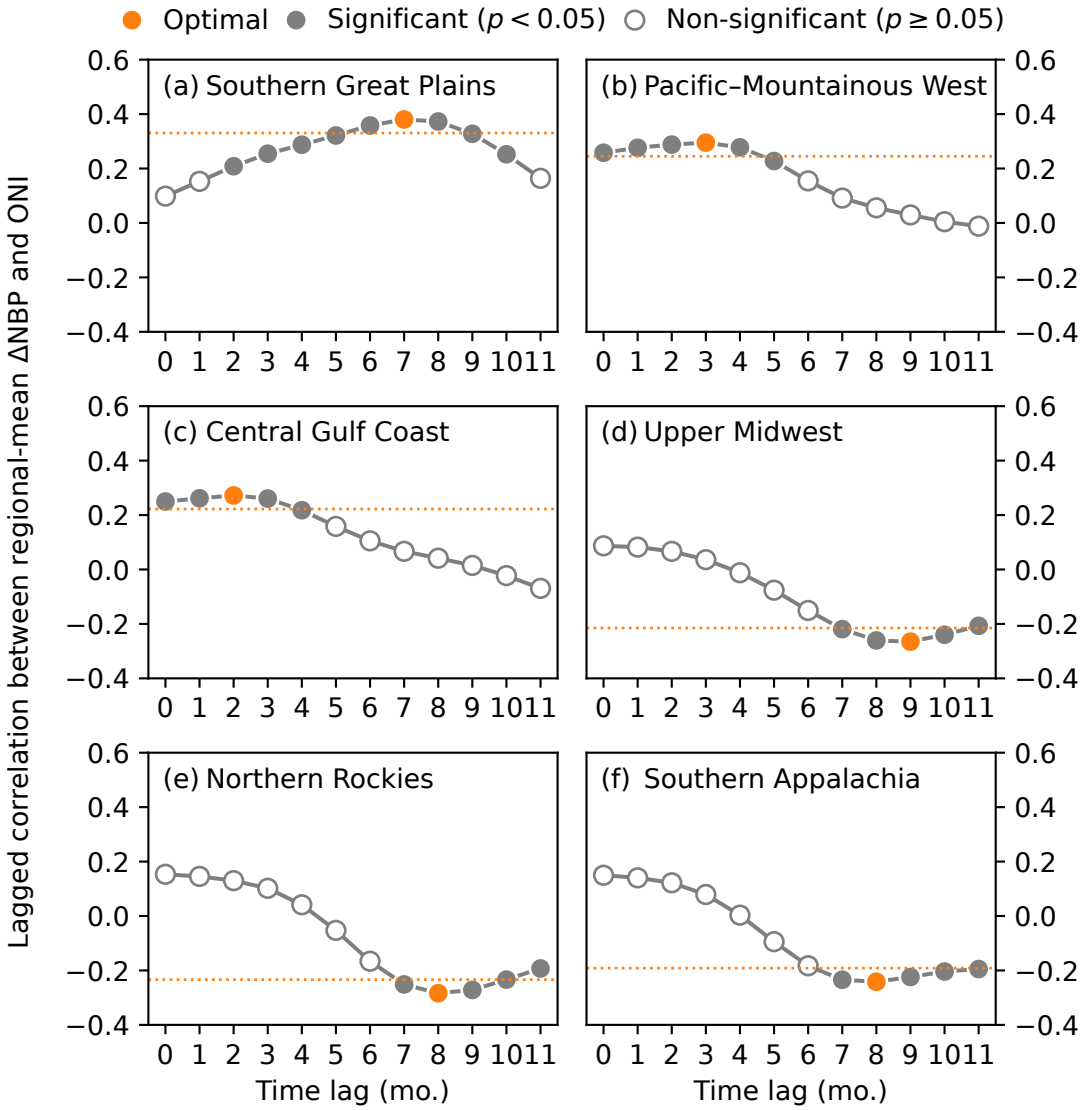

Fig. S19. Lagged correlations between regional-mean carbon uptake anomalies (ΔNBP) and the Oceanic Niño Index (ONI) for ENSO-sensitive regions. Solid circles (gray or orange) represent correlations that are statistically significant ($p < 0.05$) and empty circles represent those that are not. The optimal correlation and time lag (orange) for each region is determined by maximizing the absolute value of the cross correlation with a time lag of 0–11 months. The dashed line indicates $\Delta r = 0.05$ deviation from the optimal correlation, for assessing robustness of the optimal time lag.

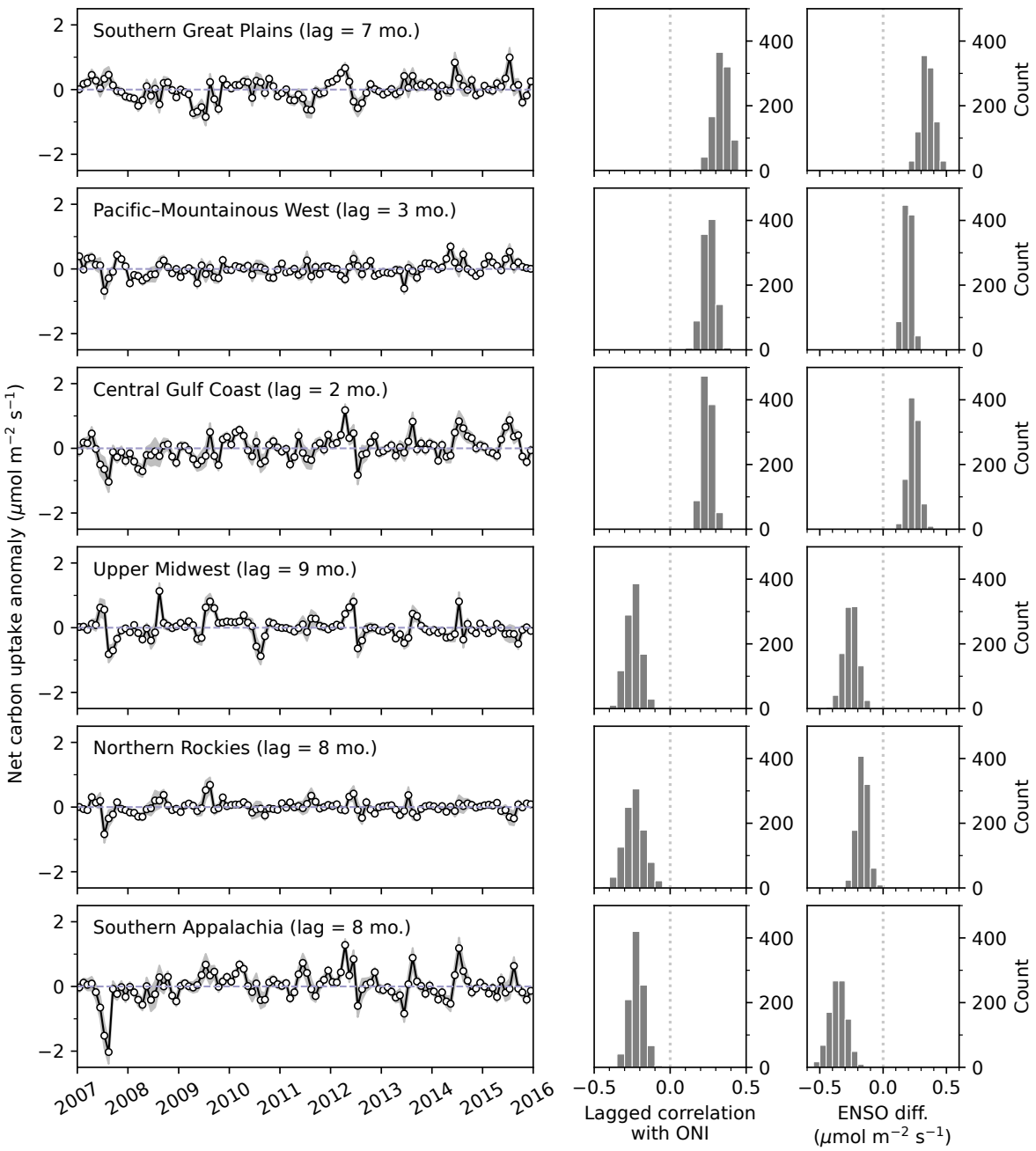

Fig. S20. Posterior uncertainty in net biome carbon uptake anomalies across temperate ENSO-sensitive regions and implications for the robustness of regional ENSO impacts. (Left column) Regional-mean monthly net carbon uptake anomalies, with $\pm 1\,\sigma$ uncertainty shown in gray shading. (Middle column) Bootstraped distribution of the lagged correlation between regional-mean monthly net carbon uptake anomalies and the Oceanic Niño Index (ONI) for each region, based on bootstrapping the uncertainty range of flux estimates for $N = 1000$ times. (Right column) Similar to the middle column but for bootstraped distribution of the ENSO composite difference (El Niño − La Niña) in net carbon uptake anomalies for each region.

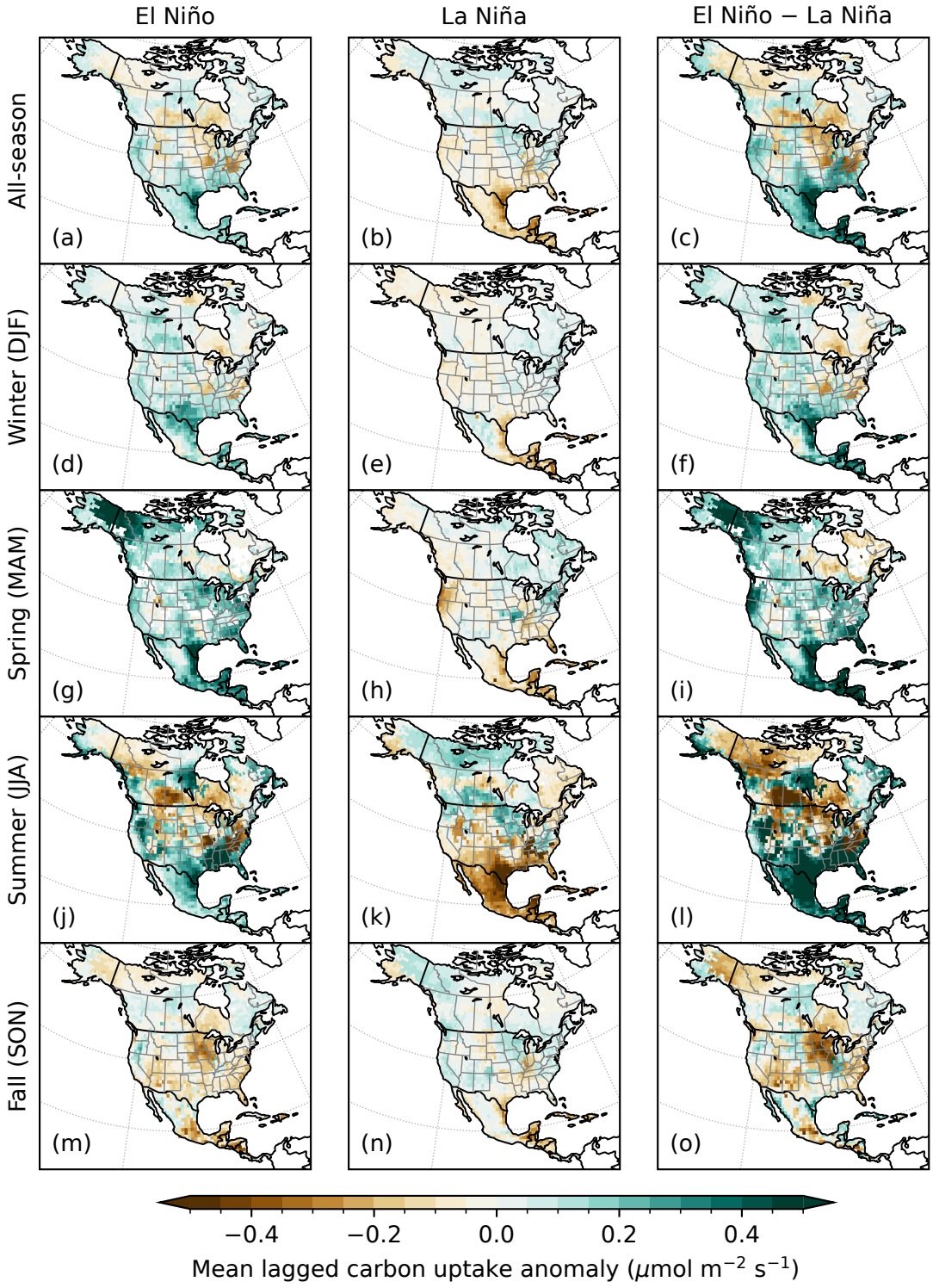

Fig. S21. Seasonal patterns of lagged net carbon uptake (i.e., net biome productivity) anomalies during El Niño (left column) and La Niña (center column) and of ENSO composite differences in net carbon uptake (right column), with the same time lags in Fig. 1a (main text) considered. Different rows indicate seasonal periods: all-season, winter, spring, summer, and fall.

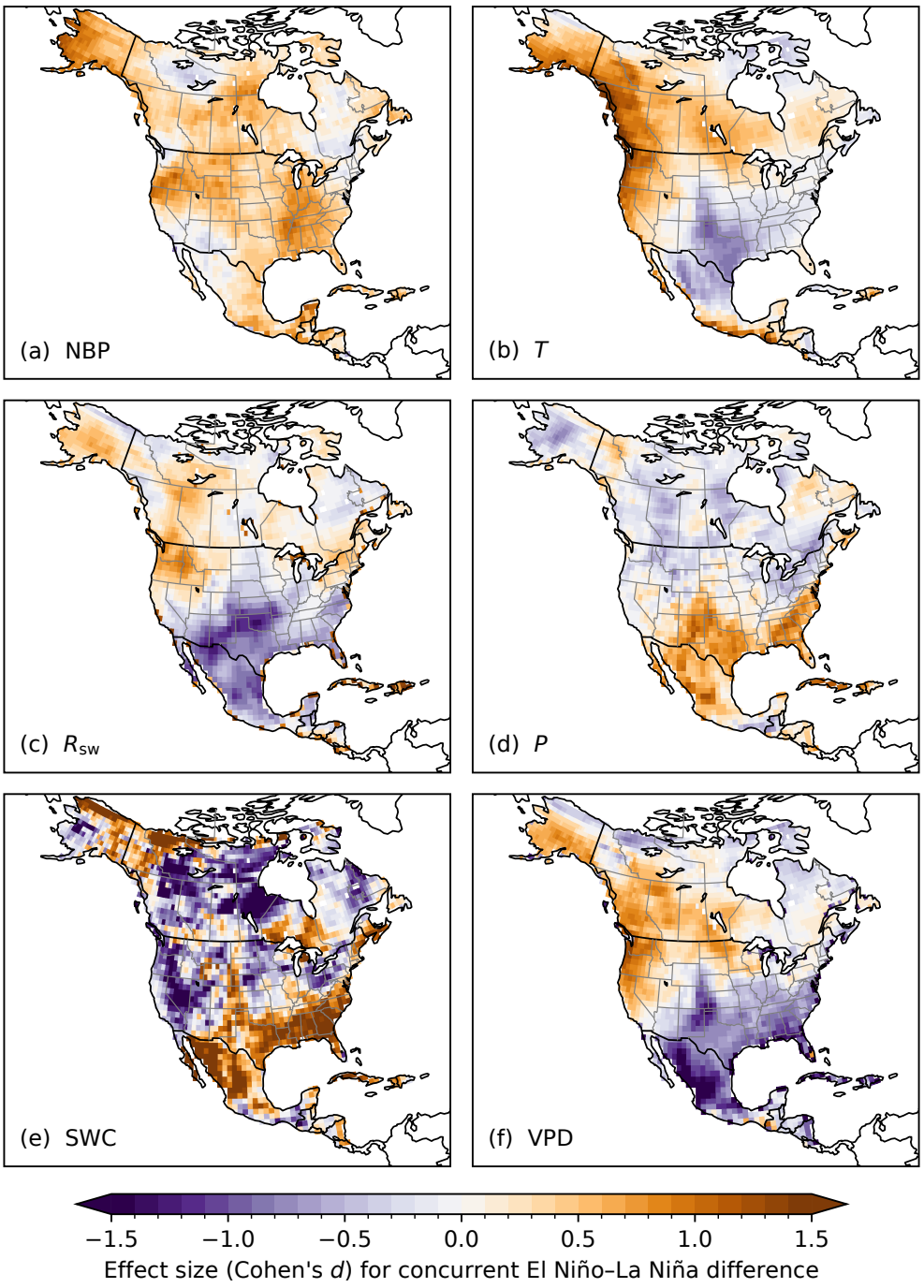

Fig. S22. Effect sizes (Cohen's d) for concurrent differences in carbon uptake anomalies and climate anomalies between ENSO phases: (**a**) net biome productivity (NBP); (**b**) air temperature (T); (**c**) incoming shortwave radiation (R_{sw}); (**d**) precipitation (P); (**e**) soil water content (SWC); (**f**) vapor pressure deficit (VPD). Similar to Fig. 5 in the main text, but *without* time lags considered.

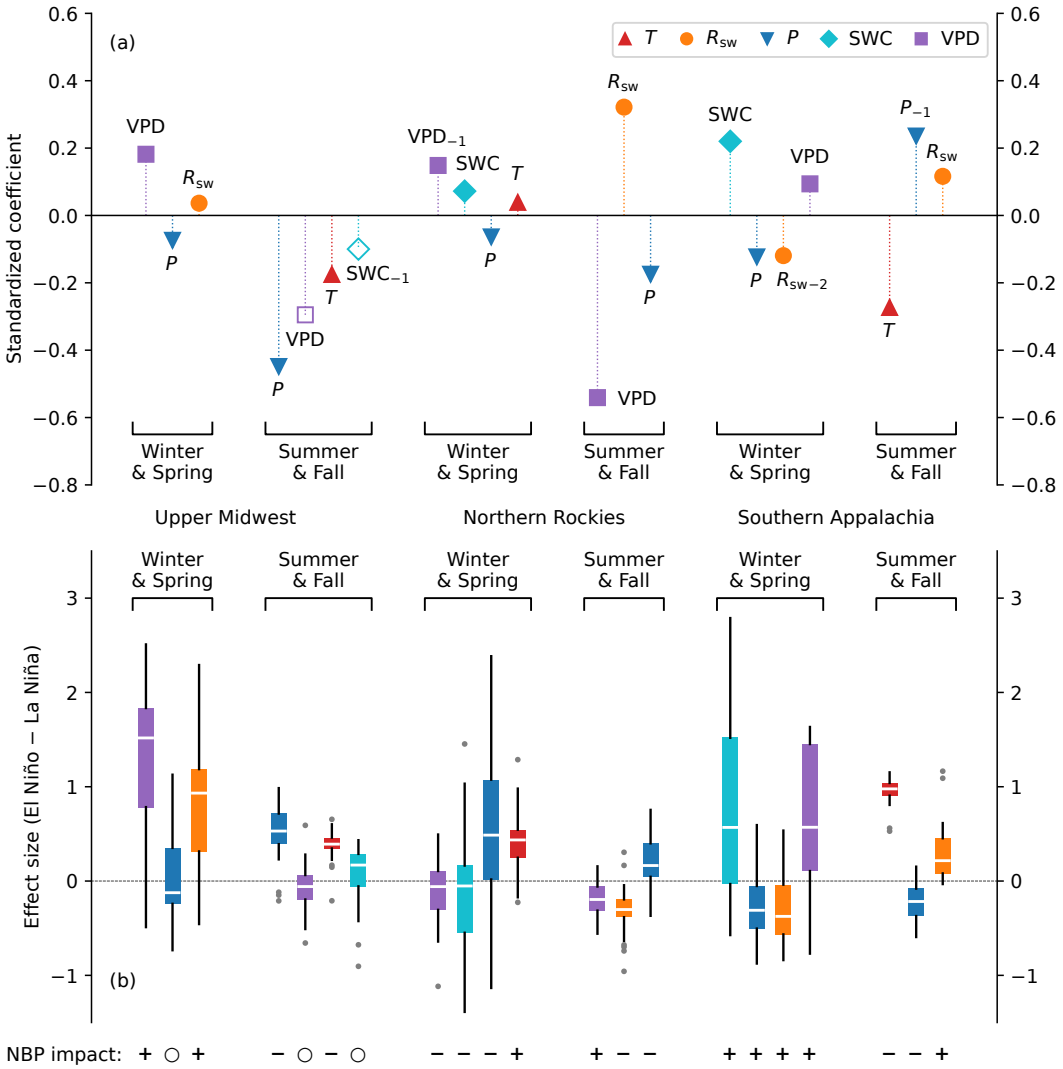

Fig. S23. Attribution of carbon uptake anomalies to climate anomalies by early (winter and spring, or December–May) and late seasons (summer and fall, or June–November) for selected ENSO-sensitive regions. (**a**) Standardized coefficients for climate anomalies in explaining carbon uptake (i.e., NBP) anomalies in each ENSO-sensitive region in a specific seasonal period, similar to Fig. 4a in the main text but divided by seasons. Empty symbols indicate variables that do not exert a robust influence on carbon uptake anomalies, as their coefficients may change sign in submodels. (**b**) Direction and relative magnitude of ENSO influences on climate anomalies in each region and seasonal period, shown in effect sizes (Cohen's *d*). Effect sizes at the grid cell level are binned as boxplots for visual assessment, with the center bar, bounds of box, whiskers, and dots representing the median, first and third quartiles, lowest and highest values falling within 1.5× of the interquartile range from the nearest quartiles and outliers beyond that range, respectively. The NBP impact of each climate variable is indicated at the bottom: a plus (minus) sign means that ENSO-induced anomalies increase (decrease) NBP, whereas a circle indicates a non-significant influence (i.e., the effect size is not significantly different from zero based on a *Z*-test).

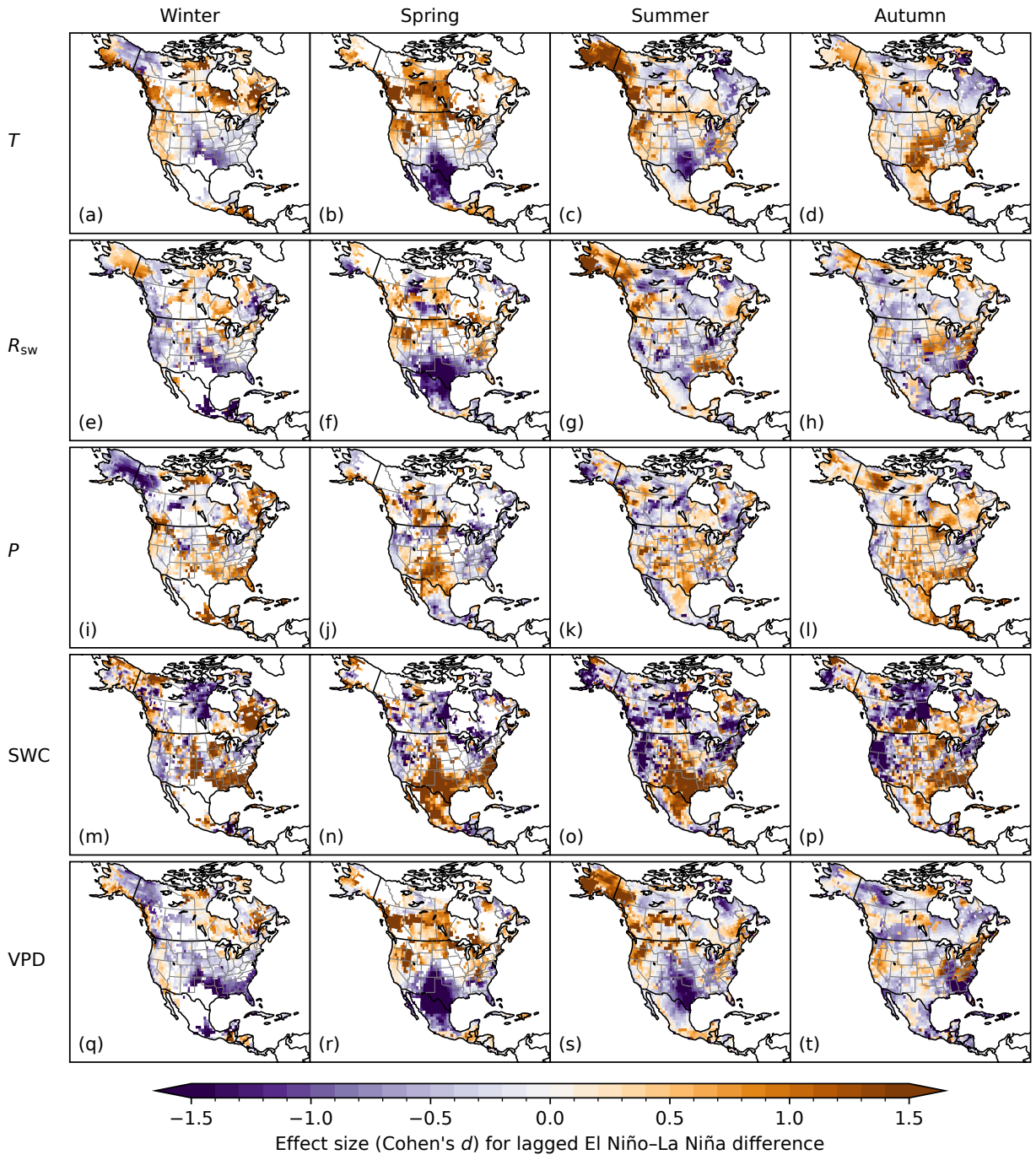

Fig. S24. Effect sizes (Cohen's d) for seasonal differences in climate anomalies between ENSO phases. Effect sizes are calculated from anomalies in air temperature (T), incoming shortwave radiation (R_{sw}), precipitation (P), soil water content (SWC), and vapor pressure deficit (VPD), grouped by El Niño- and La Niña-influenced months, with the same time lags for net carbon uptake anomalies considered (Fig. 1a in the main text). Rows indicate different climate variables and columns different climatological seasons. Blank areas in the North American domain are where there are not enough ENSO-influenced months for calculating effect sizes.

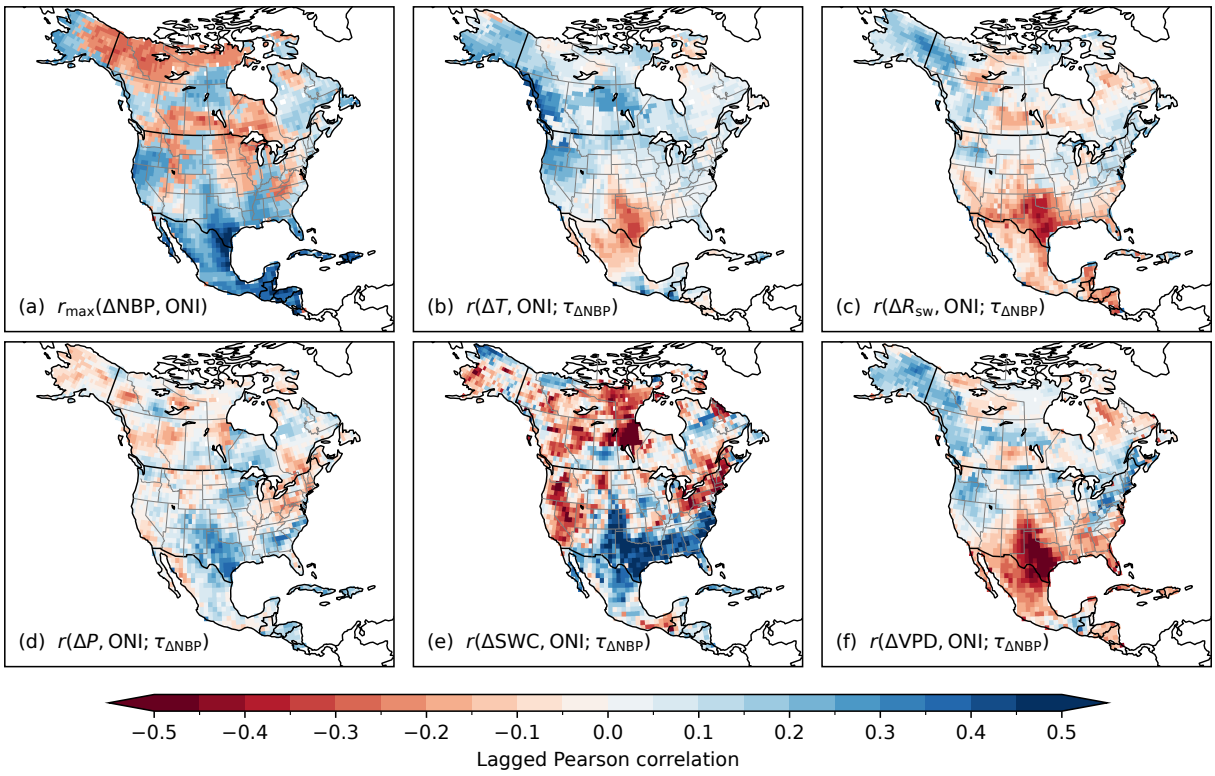

Fig. S25. Lagged Pearson correlations between climate anomalies and the Oceanic Niño Index (ONI), with the same time lags for carbon uptake anomalies considered ($\tau_{\Delta NBP}$). Also shown are the optimal Pearson correlation between carbon uptake anomalies and the ONI (**a**), same as Fig. 1b in the main text. Climate anomalies examined are those of temperature (**b**), shortwave radiation (**c**), precipitation (**d**), soil moisture (**e**), and vapor pressure deficit (**f**). Note that (**b**–**f**) differ from Fig. S12f–j because the latter is based on time lags associated with each climate variable.

References

Delire, C., Séférian, R., Decharme, B., Alkama, R., Calvet, J.-C., Carrer, D., Gibelin, A.-L., Joetzjer, E., Morel, X., Rocher, M., & Tzanos, D. (2020). The global land carbon cycle simulated with ISBA-CTRIP: Improvements over the last decade. *Journal of Advances in Modeling Earth Systems*, *12*(9), e2019MS001886. https://doi.org/10.1029/2019MS001886

Friedlingstein, P., O'Sullivan, M., Jones, M. W., Andrew, R. M., Gregor, L., Hauck, J., Le Quéré, C., Luijkx, I. T., Olsen, A., Peters, G. P., Peters, W., Pongratz, J., Schwingshackl, C., Sitch, S., Canadell, J. G., Ciais, P., Jackson, R. B., Alin, S. R., Alkama, R., Arneth, A., Arora, V. K., Bates, N. R., Becker, M., Bellouin, N., Bittig, H. C., Bopp, L., Chevallier, F., Chini, L. P., Cronin, M., Evans, W., Falk, S., Feely, R. A., Gasser, T., Gehlen, M., Gkritzalis, T., Gloege, L., Grassi, G., Gruber, N., Gürses, Ö., Harris, I., Hefner, M., Houghton, R. A., Hurtt, G. C., Iida, Y., Ilyina, T., Jain, A. K., Jersild, A., Kadono, K., Kato, E., Kennedy, D., Klein Goldewijk, K., Knauer, J., Korsbakken, J. I., Landschützer, P., Lefèvre, N., Lindsay, K., Liu, J., Liu, Z., Marland, G., Mayot, N., McGrath, M. J., Metzl, N., Monacci, N. M., Munro, D. R., Nakaoka, S.-I., Niwa, Y., O'Brien, K., Ono, T., Palmer, P. I., Pan, N., Pierrot, D., Pocock, K., Poulter, B., Resplandy, L., Robertson, E., Rödenbeck, C., Rodriguez, C., Rosan, T. M., Schwinger, J., Séférian, R., Shutler, J. D., Skjelvan, I., Steinhoff, T., Sun, Q., Sutton, A. J., Sweeney, C., Takao, S., Tanhua, T., Tans, P. P., Tian, X., Tian, H., Tilbrook, B., Tsujino, H., Tubiello, F., van der Werf, G. R., Walker, A. P., Wanninkhof, R., Whitehead, C., … Zheng, B. (2022). Global Carbon Budget 2022. *Earth System Science Data*, *14*(11), 4811–4900. https://doi.org/10.5194/essd-14-4811-2022

Haverd, V., Smith, B., Nieradzik, L., Briggs, P. R., Woodgate, W., Trudinger, C. M., Canadell, J. G., & Cuntz, M. (2018). A new version of the CABLE land surface model (Subversion revision r4601) incorporating land use and land cover change, woody vegetation demography, and a novel optimisation-based approach to plant coordination of photosynthesis. *Geoscientific Model Development*, *11*(7), 2995–3026. https://doi.org/10.5194/gmd-11-2995-2018

Hu, L., Andrews, A. E., Thoning, K. W., Sweeney, C., Miller, J. B., Michalak, A. M., Dlugokencky, E., Tans, P. P., Shiga, Y. P., Mountain, M., Nehrkorn, T., Montzka, S. A., McKain, K., Kofler, J., Trudeau, M., Michel, S. E., Biraud, S. C., Fischer, M. L., Worthy, D. E. J., Vaughn, B. H., White, J. W. C., Yadav, V., Basu, S., & van der Velde, I. R. (2019). Enhanced North American carbon uptake associated with El Niño. *Science Advances*, *5*(6), eaaw0076. https://doi.org/10.1126/sciadv.aaw0076

Ito, A. (2019). Disequilibrium of terrestrial ecosystem CO_2 budget caused by disturbance-induced emissions and non-CO_2 carbon export flows: A global model assessment. *Earth System Dynamics*, *10*(4), 685–709. https://doi.org/10.5194/esd-10-685-2019

Kato, E., Kinoshita, T., Ito, A., Kawamiya, M., & Yamagata, Y. (2013). Evaluation of spatially explicit emission scenario of land-use change and biomass burning using a process-based biogeochemical model. *Journal of Land Use Science*, *8*(1), 104–122. https://doi.org/10.1080/1747423X.2011.628705

Lawrence, D. M., Fisher, R. A., Koven, C. D., Oleson, K. W., Swenson, S. C., Bonan, G., Collier, N., Ghimire, B., van Kampenhout, L., Kennedy, D., Kluzek, E., Lawrence, P. J., Li, F., Li, H., Lombardozzi, D., Riley, W. J., Sacks, W. J., Shi, M., Vertenstein, M., Wieder, W. R., Xu, C., Ali, A. A., Badger, A. M., Bisht, G., van den Broeke, M., Brunke, M. A., Burns, S. P., Buzan, J., Clark, M., Craig, A., Dahlin, K., Drewniak, B., Fisher, J. B., Flanner, M., Fox, A. M., Gentine, P., Hoffman, F., Keppel-Aleks, G., Knox, R., Kumar, S., Lenaerts, J., Leung, L. R., Lipscomb, W. H., Lu, Y., Pandey, A., Pelletier, J. D., Perket, J., Randerson, J. T., Ricciuto, D. M., Sanderson, B. M., Slater, A., Subin, Z. M., Tang, J., Thomas, R. Q., Val Martin, M., & Zeng, X. (2019). The Community Land Model Version 5: Description of new features, benchmarking, and impact of forcing uncertainty. *Journal of Advances in Modeling Earth Systems*, *11*(12), 4245–4287. https://doi.org/10.1029/2018MS001583

Lienert, S., & Joos, F. (2018). A Bayesian ensemble data assimilation to constrain model parameters and land-use carbon emissions. *Biogeosciences*, *15*(9), 2909–2930. https://doi.org/10.5194/bg-15-2909-2018

Meiyappan, P., Jain, A. K., & House, J. I. (2015). Increased influence of nitrogen limitation on CO_2 emissions from future land use and land use change. *Global Biogeochemical Cycles*, *29*(9), 1524–1548. https://doi.org/10.1002/2015GB005086

Melton, J. R., Arora, V. K., Wisernig-Cojoc, E., Seiler, C., Fortier, M., Chan, E., & Teckentrup, L. (2020). CLASSIC v1.0: The open-source community successor to the Canadian Land Surface Scheme (CLASS) and the Canadian Terrestrial Ecosystem Model (CTEM) – part 1: Model framework and site-level performance. *Geoscientific Model Development*, *13*(6), 2825–2850. https://doi.org/10.5194/gmd-13-2825-2020

Poulter, B., Frank, D. C., Hodson, E. L., & Zimmermann, N. E. (2011). Impacts of land cover and climate data selection on understanding terrestrial carbon dynamics and the CO_2 airborne fraction. *Biogeosciences*, *8*(8), 2027–2036. https://doi.org/10.5194/bg-8-2027-2011

Reick, C. H., Gayler, V., Goll, D., Hagemann, S., Heidkamp, M., Nabel, J. E. M. S., Raddatz, T., Roeckner, E., Schnur, R., & Wilkenskjeld, S. (2021). *JSBACH 3 - the land component of the MPI Earth System Model: Documentation of version 3.2* (Berichte zur Erdsystemforschung (Reports on Earth System Science) No. 240). Max-Planck-Institut für Meteorologie. Hamburg, Germany. https://doi.org/10.17617/2.3279802

Sitch, S., O'Sullivan, M., Robertson, E., Friedlingstein, P., Albergel, C., Anthoni, P., Arneth, A., Arora, V. K., Bastos, A., Bastrikov, V., Bellouin, N., Canadell, J. G., Chini, L., Ciais, P., Falk,

S., Harris, I., Hurtt, G., Ito, A., Jain, A. K., Jones, M. W., Joos, F., Kato, E., Kennedy, D., Klein Goldewijk, K., Kluzek, E., Knauer, J., Lawrence, P. J., Lombardozzi, D., Melton, J. R., Nabel, J. E. M. S., Pan, N., Peylin, P., Pongratz, J., Poulter, B., Rosan, T. M., Sun, Q., Tian, H., Walker, A. P., Weber, U., Yuan, W., Yue, X., & Zaehle, S. (2024). Trends and drivers of terrestrial sources and sinks of carbon dioxide: An overview of the TRENDY project. *Global Biogeochemical Cycles*, *38*(7), e2024GB008102. https://doi.org/10.1029/2024GB008102

van der Werf, G. R., Randerson, J. T., Giglio, L., van Leeuwen, T. T., Chen, Y., Rogers, B. M., Mu, M., van Marle, M. J. E., Morton, D. C., Collatz, G. J., Yokelson, R. J., & Kasibhatla, P. S. (2017). Global fire emissions estimates during 1997–2016. *Earth System Science Data*, *9*(2), 697–720. https://doi.org/10.5194/essd-9-697-2017

Vuichard, N., Messina, P., Luyssaert, S., Guenet, B., Zaehle, S., Ghattas, J., Bastrikov, V., & Peylin, P. (2019). Accounting for carbon and nitrogen interactions in the global terrestrial ecosystem model ORCHIDEE (trunk version, rev 4999): Multi-scale evaluation of gross primary production. *Geoscientific Model Development*, *12*(11), 4751–4779. https://doi.org/10.5194/gmd-12-4751-2019

Walker, A. P., Quaife, T., van Bodegom, P. M., De Kauwe, M. G., Keenan, T. F., Joiner, J., Lomas, M. R., MacBean, N., Xu, C., Yang, X., & Woodward, F. I. (2017). The impact of alternative trait-scaling hypotheses for the maximum photosynthetic carboxylation rate (V_{cmax}) on global gross primary production. *New Phytologist*, *215*(4), 1370–1386. https://doi.org/10.1111/nph.14623

Wiltshire, A. J., Burke, E. J., Chadburn, S. E., Jones, C. D., Cox, P. M., Davies-Barnard, T., Friedlingstein, P., Harper, A. B., Liddicoat, S., Sitch, S., & Zaehle, S. (2021). JULES-CN: A coupled terrestrial carbon–nitrogen scheme (JULES vn5.1). *Geoscientific Model Development*, *14*(4), 2161–2186. https://doi.org/10.5194/gmd-14-2161-2021

Yuan, W., Liu, D., Dong, W., Liu, S., Zhou, G., Yu, G., Zhao, T., Feng, J., Ma, Z., Chen, J., Chen, Y., Chen, S., Han, S., Huang, J., Li, L., Liu, H., Liu, S., Ma, M., Wang, Y., Xia, J., Xu, W., Zhang, Q., Zhao, X., & Zhao, L. (2014). Multiyear precipitation reduction strongly decreases carbon uptake over northern China. *Journal of Geophysical Research: Biogeosciences*, *119*(5), 881–896. https://doi.org/10.1002/2014JG002608

Yue, X., & Unger, N. (2015). The Yale Interactive terrestrial Biosphere model version 1.0: Description, evaluation and implementation into NASA GISS ModelE2. *Geoscientific Model Development*, *8*(8), 2399–2417. https://doi.org/10.5194/gmd-8-2399-2015

Zaehle, S., & Friend, A. D. (2010). Carbon and nitrogen cycle dynamics in the O-CN land surface model: 1. model description, site-scale evaluation, and sensitivity to parameter estimates. *Global Biogeochemical Cycles*, *24*(1), GB1005. https://doi.org/10.1029/2009GB003521